Chapter 4

Solar hot water storage tanks. Thermal stratification analysis by means of detailed numerical simulations

Abstract. The aim of this chapter is the study of thermal stratification of storage tanks by means of detailed numerical simulations. Two situations are considered: i) the transient thermal behaviour of a horizontal storage tank forming part of a thermosyphon solar heating system, during its unloading process and, ii) the transient behaviour of a vertical storage tank with a manifold diffuser under different load conditions. The current state-of-the-art in the analysis of stratified storage tanks is briefly reviewed and a new exergy-based parameter is proposed in order to quantify the thermal stratification inside the storage. The current computational possibilities of three-dimensional Computational Fluid Dynamics (CFD) simulations, using loosely coupled parallel computers (Beowulf clusters) in the *virtual prototyping* of thermal storage tanks is also shown. Special attention is given to the validation of the assumed mathematical model, the verification of the numerical solutions, and the post-processing tasks carried out in order to quantify the level of thermal stratification. The computational possibilities and limitations of this kind of detailed numerical simulations are pointed out. Most of the material here presented has been published as [1].

4.1 Introduction

The loss of stratification in liquid thermal storage tanks is associated with several factors: the mixing induced by the inlet streams from collector (heat source) or load (cold source) loops, the heat transfer that may occur through the tank envelope and insulation, the heat diffusion in the water through the different layers of the fluid and in the solid parts, among others. The mixing due to the fluid streams entering the tank either from heat source or from cold source, is with difference, the major contribution to the degradation of the thermal stratification. In this sense, several numerical and experimental studies that analyse various alternatives so as to preserve the thermal stratification can be found in the literature [2, 3, 4].

Usually, the stratification of a thermal storage is represented by the transient temperature profiles under different thermal, fluid dynamic and geometric conditions. However, quantitative measurements of the level of temperature stratification appear to be an attractive tool for reporting possible improvements in the optimisation process of these devices in a compact manner. In the last decade, different parameters to quantify the degree of thermal stratification have been defined and can be found in the literature. The most illustrative ones are hereafter reviewed.

Bahnflet and Musser [3, 5, 6] calculated an equivalent loss of capacity (or equivalent loss of tank height) evaluating the capacity lost due to mixing and conduction during the course of a cycle (charging and discharging). The lost capacity is defined as the capacity that cannot be removed from a tank due to an outlet temperature limitation.

They also used the thermocline thickness as an illustrative parameter to characterise the temperature distribution inside the tanks [5]. The thermocline thickness is defined as the vertical region of fluid inside the tank which contains a thermal transition layer between warm and cool water volumes. Evaluating the non-dimensional temperature like in Eqn. (4.1), the thermocline thickness (h_t) can be defined as the distance between the tank positions for which $0.9 \leq \Theta \leq 0.1$.

$$\Theta = \frac{T - T_c}{T_h - T_c} \tag{4.1}$$

Although a thicker thermocline is associated with a larger degradation of stratification, this parameter does not reflects how large this degradation is. Furthermore, this measure can only be used for storages with constant inlet temperature in which a well-defined thermocline region is present. Thus, it is not appropriated for most of the situations encountered in solar water systems where the temperature of the heat source varies continuously along the time.

Davidson et al. [7] and Adams and Davidson [8] proposed a way to measure the level of temperature stratification by weighting the energy stored by its vertical location (which is similar to an energetic momentum).

The dimensionless energetic momentum defined as MIX number is calculated as a function of the largest and smallest values of the energetic momentum (considering ideally fully stratified tank and completely mixed tank). These ideal situations are evaluated using analytical models. The completely mixed tank situation is obtained by means of a global energy balance in the tank, while the plug flow model [9], is used to predict tank temperature distribution for the fully stratified situation.

$$MIX = \frac{M_{st} - M}{M_{st} - M_{mix}} \tag{4.2}$$

Although this parameter considers the transient nature of the inlet profile, it is only useful when the relative performance of different designs under the same mass flow rate and thermal conditions are compared. This parameter fails in the comparison between different load (or unload) strategies for the same geometry.

Various works in the literature report that an energy analysis could not be sufficient to compare different temperature distributions [10, 11, 12, 13, 14]. Energy analysis can not distinguish between tanks with different levels of temperature, even if these tanks have equivalent energy quantities, i.e. energy analysis can not account for the degradation of the energy stored. In this sense, the Second Law of Thermodynamics provides an alternative way to evaluate the quality of the stored energy. The process of loss of stratification (due to fluid mixing, environment losses, etc.) creates entropy and, by consequence, a degradation of the energy stored. Exergy analysis can be then a tool for evaluating this degradation, quantifying its quality. The works carried out by Rosen [11, 12, 15, 13] are an example of this kind of analysis. In his works, he has defined an exergy efficiency over a closed system, considering both charging and discharging processes. Exergy efficiency is then defined as the ratio of the exergy of the discharge process to the charge process. This parameter shows the importance of temperature stratification in the performance of the storage tank. The higher the storage stratification, the higher the value of the exergy efficiency. However, this parameter is only useful after a complete cycle of charging and discharging of the store, being difficult to consider the transient nature of the process.

In the present chapter, the stratification process of storage tanks used in solar thermal systems is under study. Two different situations have been considered: i) the influence of the inlet mass flow rate in the stratification of an horizontal storage tank of a thermosyphon water system during its unloading phase and, ii) the influence of the inlet and initial conditions of the storage during the loading process of a vertical storage tank with a manifold stratifier. To carry out the study, both situations have been tested virtually by means of detailed multidimensional computational fluid dynamics (CFD). The results of the numerical experiments have been post-processed in order to quantify the level of stratification. From the analysis performed, a new exergy-based non-dimensional parameter has been proposed.

The exergy-based parameter quantify the degree of thermal stratification referred to the ideal limit situations: a fully stratified storage tank without heat diffusion between fluid layers and a fully-mixed tank. Comparisons with the current state-of-the-art available strategies to quantify stratification inside the tank have been also shown.

The current computational possibilities of these kind of simulations, using different techniques such as loosely coupled parallel computing (Beowulf clusters), as a tool for *virtual prototyping* of thermal storage tanks have been also pointed out.

4.2 Measure of the degree of thermal stratification

In order to quantify the level of thermal stratification in a storage tank, an exergy-based analysis is hereafter described. Instantaneous exergy of the fluid inside a storage tank can be evaluated as:

$$\Xi = \int_{\Omega} \xi \, \rho \, d\Omega \tag{4.3}$$

where the specific exergy (also called flow availability) neglecting kinetic and potential exergy is obtained from:

$$\xi = (h - h_o) - T_o(s - s_o) \tag{4.4}$$

Enthalpy and entropy at the dead state are indicated with the subindex "o". The reference dead state corresponds to the state of thermodynamic equilibrium with the natural surroundings.

The ideal limit situations, the completely mixed and the fully-stratified storage models, can provide limiting values for an exergy-based analysis. In the fully-stratified model [9], the tank is divided into a number of uniform temperature layers. The fluid streams entering the tank are assumed to be placed at the temperature level most closest in temperature without exchanging heat with the adjacent fluid layers or those along their path. That is, over a fixed time step, as a volume of water enters the tank, it is placed at the vertical location which ensures no temperature inversion. At the same time, the same volume of water is removed from the bottom (or the top, depending if a load or unload process is considered). After account for the fluid entering the tank, an energy balance at each fluid layer is carried out to consider energy losses to the surroundings. Thus, the temperature at the ith fluid layer can be evaluated by the following equation:

$$\rho_i c_{p\,i} \Omega_i \frac{dT_i}{dt} = -(U\,S)_i (T_i - T_{env}) \tag{4.5}$$

On the other hand, the fully-mixed model considers that the entire tank has a uniform temperature (T_{mix}) which change in time due to energy losses to the ambient or due to a net energy addition or withdrawal during the load or unload phases. The energy balance accounting for these factors gives:

$$\rho c_p \Omega \frac{dT_{mix}}{dt} = \dot{m}_{in} c_{p\,in} (T_{in} - T) - U\,S(T_{mix} - T_{env}) \tag{4.6}$$

Once the temperature distribution of the ideal limit situations are known, and based on the exergetic levels of the tank (at the already mentioned ideal limit situations), a non-dimensional exergy can be defined as:

$$\xi^* = \frac{\Xi_{st} - \Xi}{\Xi_{st} - \Xi_{mix}} \tag{4.7}$$

or in an equivalent form as:

$$\xi^* = 1 - \frac{\Xi - \Xi_{mix}}{\Xi_{st} - \Xi_{mix}} \tag{4.8}$$

The non-dimensional exergy equals zero for a tank with a temperature distribution identical to that predicted by a fully stratified model, and it equals 1 if the fluid inside the tank is totally mixed.

Considering both, density and specific heat constant, the global instantaneous exergy difference in the actual tank and in a completely mixed tank can be evaluated as:

$$\Xi - \Xi_{mix} = \sum_{cv} c_p\,(T_i - T_{mix})\rho\,\Omega_i - T_o \sum_{cv} c_p\,ln\,(T_i/T_{mix})\rho\,\Omega_i \tag{4.9}$$

where the summation is extended to all the CVs into which the fluid is discretised. T_{mix} is obtained by means of the global energy balance (Eqn. 4.6).

Alternatively, Eqn. (4.9) can be rewritten as:

$$\Xi - \Xi_{mix} = c_p\,[(\overline{T} - T_{mix}) - T_o\,ln\,(\widetilde{T}/T_{mix})]\rho\,\Omega \tag{4.10}$$

where being $\Omega = \sum_{cv} \Omega_i$:

$$\overline{T} = \frac{1}{\Omega} \sum_{cv} T_i \Omega_i \tag{4.11}$$

and

$$\widetilde{T} = exp\left[\frac{1}{\Omega} \sum_{cv} \Omega_i\,ln\,T_i\right] \tag{4.12}$$

In a similar manner, the exergy change considering a fully-stratified and a completely mixed tank, $\Xi_{st} - \Xi_{mix}$, can be evaluated from Eq. (4.10). In this case, $\overline{T}_{st}$ and $\widetilde{T}_{st}$ are evaluated as follows:

$$\overline{T}_{st} = \frac{1}{\Omega} \sum_{cv} T_{st,i} \Omega_i \tag{4.13}$$

and

$$\widetilde{T}_{st} = exp \left[\frac{1}{\Omega} \sum_{cv} \Omega_i \; ln \, T_{st,i} \right] \tag{4.14}$$

where $T_{st,i}$, which only depends on the vertical coordinate, is evaluated by using the fully-stratified model.

4.3 Definition of the cases

In order to study and quantify the level of stratification of storage tanks, two different situations have been considered: i) the unloading process of a horizontal storage tank (commonly used in thermosyphon solar water systems) under the influence of different mass flow rates and, ii) the loading process of a vertical storage tank with a manifold stratifier under different initial and inlet temperature conditions.

4.3.1 Unloading phase case

With regard to the unloading processes, the mass flow rate delivered to the load depends on the hourly load profiles. Often, daily loads are approximately one renovation of the tank per day. Usually, the maximum requirement for consumption is about $20 - 30\%$ of the total daily mass flow rate [16, 17]. Considering a domestic hot water system with a $4 \, m^2$ collector area and a $0.3 \, m^3$ storage tank (~ 300 l), the peak mass flow rate could be around $0.0167 - 0.025$ kg/s ($\sim 60 - 90$ l/h), sometimes even larger. These peaks of cold water entering the tank can affect its thermal stratification adversely.

In this chapter, the influence of the inlet mass flow rate from the load loop on the degree of thermal stratification in a storage tank forming part of a thermosyphon water heating system has been analysed virtually. The experimental set-up constructed by Alizadeh [4] and his results have been considered. The device tested in his work has been a horizontal tank made of Plexiglas material (chosen so as to allow the visualisation of the mixing process inside the tank). The top half of the tank has been externally insulated by fibreglass material. The tank length (H) has been 1.5 m with an internal diameter (D) of 0.5 m. The Plexiglas material has been 5 mm thick, and

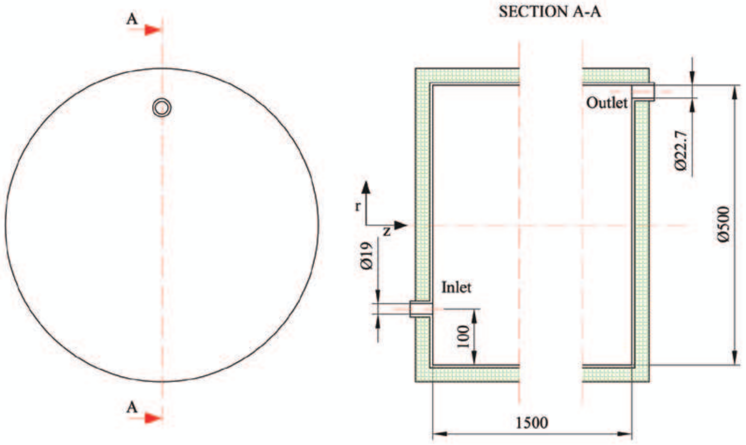

Figure 4.1: Problem definition. Unloading phase case. Storage tank geometry (chassis thickness 5mm, insulation thickness 25.4 mm).

the thermal insulation of 25.4 mm thick. At both ends of the tank, there were two inlet/outlet ports for connection to the solar system. For geometrical details, see Fig. 4.1.

Alizadeh [4] experimentally studied the thermal behaviour of the tank and, based in the experimental results, proposed a one-dimensional model that accounts for the mixing effects at the inlet region. Among other aspects, he analysed the unloading process of the tank and pointed out the influence of different kinds of inlet nozzles (e.g., straight tubes versus divergent conical tubes).

In this chapter, attention is paid to the unloading process using a straight tube at the inlet. Reproducing the experimental conditions of [4], the tank has been considered with an initial constant warm temperature of 42 °C. Cold water (20 °C) has been injected at one of the ends of the tank (100 mm from the bottom). In order to study the influence of the mass flow rate in the formation of the thermocline and in degradation of stratification, four mass flow rates have been considered: 0.0167, 0.025, 0.05 and 0.1 kg/s (i.e., $\sim 60, 90, 180$ and 360 l/h).

4.3.2 Loading phase case

The loading process of a vertical storage tank with a manifold diffuser under different situations has been considered. The selected tests have been proposed by Davidson et al. [7]. In their work, they have compared experimentally, two different kind

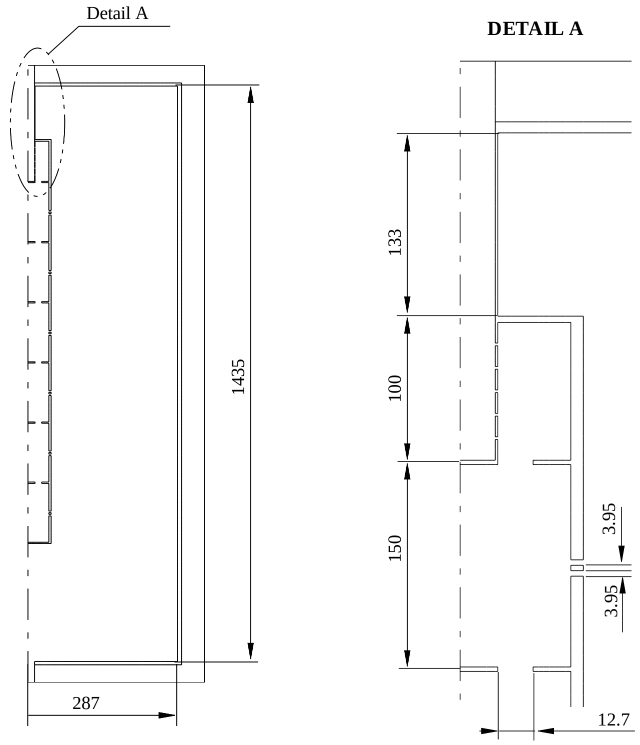

Figure 4.2: Problem definition. Loading phase case. Tank geometry and stratification manifold details.

of inlets: a drop-tube inlet and a stratification manifold. For both geometries, three different initial and inlet temperature situations have been analysed. In the work, the comparison of the performance of each kind of inlet has been based on the *MIX* number commented before.

In order to study the load process of the tank, the development of the thermocline and the degradation of the stratification due to the inlet conditions of the fluid, the three tests proposed in [7] have been reproduced numerically.

For the virtual tests, the tank considered has been made of $8mm$ polycarbonate material with a volume of $0.372m^3$ ($\sim$ 372 l) and an aspect ratio (H/D) of 2.5. The tank has been externally insulated with $44mm$ thick fibreglass material. The rigid

test	Initial temperature $[^{\circ}C]$	Inlet temperature $[^{\circ}C]$	Test duration $[min]$
Test 1	half top tank: 50 half bottom tank: 20	30	48
Test 2	20	50	90
Test 3	20	variable (see table 4.2)	90

Table 4.1: Problem definition. Loading phase case. Test conditions.

manifold has been made also of polycarbonate with an inlet diameter of $89mm$, and the inlet section of the manifold has a diameter of $25.4mm$. The outlet diameter of the tank has been also of $25.4mm$. The stratifier, similar to the used by Davidson et al. [18], has consisted of a diffuser that reduces the inlet stream momentum and, a manifold distributor with several outlet orifices that force the fluid to exit at the height most closest to its temperature. Details about the geometry of the tank and the manifold are shown in Fig. 4.2. The storage tank and manifold geometries adopted have been similar to those studied by [18]. However, some differences can be encountered due to a lack of data in the description of the experimental set-up in [18]. Although tank volumes are the same, aspect ratio, insulation thickness and material have been assumed in the present study. Furthermore, even when experimental tests have been defined in their work, uncertainties in initial and inlet conditions have been found. Thus, the numerical study conducted here does not pretend to be an exact reproduction of the mentioned work, but a study of the thermal stratification behaviour in this kind of geometry by means of the tests proposed in [18].

In the tests carried out, the mass flow rate has been fixed to $0.07l/s$, which is in correspondence with usual mass flow rates from collector loop in solar water systems (about $0.01-0.02$ kg/sm^2 of collector area). As the tank is charged the same mass flow rate is withdrawn from the bottom of the tank. The initial and inlet conditions for each test situation are summarised in Tables 4.1 and 4.2.

4.4 Some remarks about the numerical approach

4.4.1 Unloading phase case

The initial and boundary conditions have been adjusted to the defined problem in section 4.3.1. The initial temperature of the whole tank has been set to 42 °C. A mass flow rate of cold water at 20 °C then, has entered the tank. The ambient temperature has been fixed at 23 °C. The thermal loss of the tank has been modelled consider-

time [min]	$T_{in} [^\circ C]$
0-10	50
10-20	40
20-30	30
30-40	30
40-50	40
50-60	50
60-70	40
70-80	30
80-90	40

Table 4.2: Problem definition. Loading phase case. Inlet temperature profile for Test 3.

	Material		
Property	Water	Plexiglas	Insulation
$\rho\,[kg/m^3]$	996.2	262	60
$c_p\,[J/kgK]$	4164.4	1050	960
$k\,[W/mK]$	0.6155	0.17	0.038
$\mu\,[Pa\,s]$	$8.07\,10^{-4}$		
$\beta\,[1/K]$	$2.76\,10^{-4}$		

Table 4.3: Computational aspects. Thermo-physical properties for the unloading phase case.

ing standard correlations for mean heat transfer coefficients in isothermal horizontal cylinders and vertical lateral walls [19]. At the outlet, the injected mass flow rate has been also imposed, and the temperature derivative has been assumed to be null. The thermo-physical properties used are listed in Table 4.3.

Because of the symmetrical location of the inlet/outlet ports, the computational domain selected has accounted for half of the tank. The full tank has been considered to be insulated. The inlet/outlet ports have been adapted geometrically. The size of the control volumes (CVs) has been maintained constant throughout the domain, except for the zones accounting for the tank's chassis and its insulation. The computational grid has been composed of n_rxn_θxn_z CVs. The simulated time has been discretised using a constant time increment Δt. For each time step, the iterative convergence procedure has been truncated once the non-dimensional mass and energy balances (normalised by the total mass of water inside the tank and the inlet enthalpy flux respectively) have been lower than 0.01, or if the number of outer

Property	Material Water	 polycarbonate	 Fibre-glass
$\rho\,[kg/m^3]$	994.862	1250	32
$c_p\,[J/kgK]$	4162.26	1210	835
$k\,[W/mK]$	0.6217	0.20	0.038
$\mu\,[Pa\,s]$	$7.341\ 10^{-4}$		
$\beta\,[1/K]$	$3.154\ 10^{-4}$		

Table 4.4: Thermo-physical properties for the loading phase case.

iterations has been greater than 40.

In the present study, an *h-refinement* procedure has been performed in order to verify the numerical solutions. Numerical schemes have been fixed in order to analyse the influence of the mesh spacing and time increment on the numerical solutions obtained. Three computational meshes of 15x16x34, 30x32x68, 60x64x136 CVs have been considered. The simulation time has been discretised in time increments of 0.1, 1.0 and 10 seconds. Results about the *h-refinement* process and the final discretisation adopted are discussed in further sections.

4.4.2 Loading phase case

According with the definition of the different tests given in section 4.3.2, the initial and boundary conditions have been adjusted. At the inlet and outlet, the mass flow rate has been imposed equal to $0.07l/s$. Inlet temperature has been fixed according with Tables 4.1 and 4.2, while at the outlet, temperature derivative has been assumed null. The ambient temperature has been fixed to $20°C$ and the external heat transfer coefficient has been assumed $10W/m^2K$. Thermophysical properties for each material are given in Table 4.4.

Considering the configuration of the case, the computational domain has been assumed to be axisymmetric. The size of the control volumes has been approximately maintained constant, except for the zones near the manifold where the geometry imposes an irregular distribution of the control volumes. An example of the mesh distribution is shown in Fig. 4.3. The simulation time has been also discretised using constant time increments of Δt. For each time step, the iterative loop has been stopped once the non-dimensional mass and energy balances have been lower than 10^{-5}, or if the number of outer iterations has been greater than 30.

In order to analyse the influence of the mesh spacing in the numerical solution, three different meshes of 53x191, 87x229 and 174x458 have been considered. Notice that, in order to describe properly the geometry of the manifold diffuser, a large

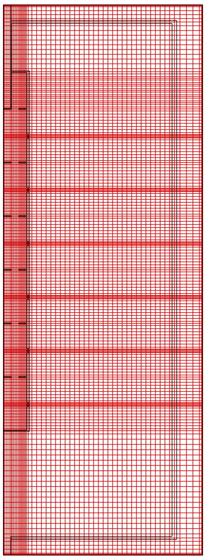

Figure 4.3: Computational aspects. Example of the computational mesh for the loading phase case. 53x191 CV mesh.

number of CVs have been used in the axial direction. For the time discretisation, time steps of 0.05, 0.1 and 1 seconds have been considered. The results of the verification of the solutions using the different space and time discretisation are discussed in further sections.

4.4.3 Parallel multi-block algorithm

Three-dimensional transient CFD and heat transfer simulations using standard algorithms [20] (such as the ones presented in this chapter) are computationally very costly. Previous experiences in the study of the phenomena taking place in storage tanks [21, 22], shown that the resolution of three dimensional domains could be very expensive in terms of time and computational resources. Considering the unloading process simulated in this chapter, and the highest level of refinement (i.e. 60x136x64 CV), about 3 million equations must be discretised and solved iteratively for each time increment. It is estimated that a standard PC running at 1900 MHz will take around 3-4 days of CPU time to obtain a numerical solution. This may be considered disappointing if this kind of numerical simulation is expected to be used as an alternative tool in the thermal optimisation of storage tanks.

Taking advantage of the emergence of the *Beowulf clusters*, the development of parallel algorithms specially designed to be performed in these computational infrastructures, seems to be an attractive choice in order to reduce the computational cost commented above with an acceptable budget.

The parallel multi-block algorithm used in this chapter has been specially conceived to compute fluid flows with a clear parabolic structure [23]. In fact, the information transfer among the different blocks has been made in an explicit manner. This could suppose an inefficient resolution of elliptic problems. The algorithm has been previously used to solve steady-state problems such as the numerical simulation of steady-state laminar flames [24], and in the transient numerical simulation of ventilated facades [25]. In the first case, the parabolic structure of the flow clearly benefit the algorithm's performance. In the second case, although the flow has a global parabolic structure, the inner geometry of the facade also produced a considerable complex flow inside the channel. Nevertheless, in both situations, the efficiency of the algorithm has been very promising. These results have been a motivation for test it in this kind of problems.

In the multi-block method, the discretised domain has been divided into several overlapping blocks joined by interpolation schemes [26]. The resulting algebraic systems of equations have been solved for each block (inner iteration). Once all blocks have been calculated, information of the interpolation schemes has been transferred among the different blocks in an explicit manner (outer iteration). This strategy has allowed the simultaneous solving of several blocks by different CPUs. The processors communicated only once per outer iteration. Therefore, the communication work has been notably less costly than the calculation work. This factor benefits the use of the proposed algorithm in *Beowulf clusters*. For more details on the parallel implementation of the code see [23].

An illustrative example of how the multi-block method has been applied can be seen in Fig. 4.4. The computational mesh has been split into two blocks along the axial direction. As can be seen, the length of the blocks has been extended with 2 CVs, in order to define the overlapping zone where the information transfer has been applied. Four CVs have been selected to define these zones in order to maintain the accuracy of the numerical solutions (please note that third-order schemes have been employed to evaluate convective terms).

Due to the definition of the overlapping zones, the total number of CVs for a multi-block discretisation is defined by the following equation:

$$CV_N = CV_1 + 4\,(N-1)\,n_r\,n_\theta \tag{4.15}$$

where CV_N, is the total number of control volumes for a multi-block discretisation

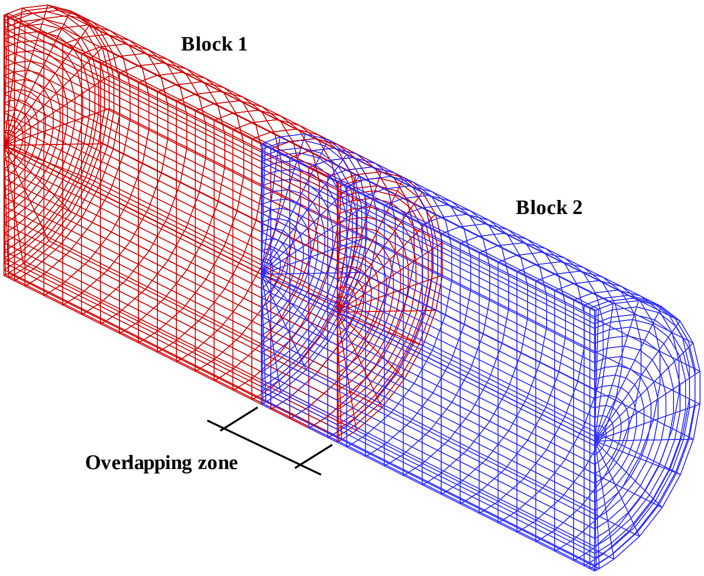

Figure 4.4: Illustrative example of multi-block discretisation. Computational domain split into two blocks. Definition of the overlapping zone.

with N blocks, and CV_1 is the number of control volumes for the single block discretisation. The increase in the number of CVs is a key factor to be taken into account when selecting the number of blocks (there is a maximum for a given discretisation), and when estimating the computational savings resulting from parallelisation.

Computational aspects

Before discussing the computational factors related to the efficiency of the algorithm in the numerical simulation of the unloading storage tanks processes, some of the main aspects that affect its use should be mentioned: i) the explicit treatment of the interpolated boundaries should have a negligible impact on the number of global outer iterations to converge a time-step; ii) the amount of work carried out for each processor involved in the resolution should be similar (good load balances); iii) the communication load between the processors involved should be smaller than their

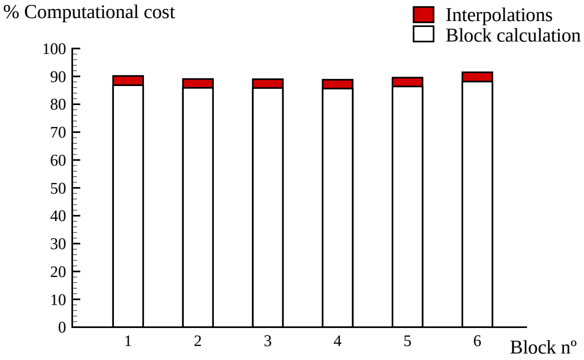

Figure 4.5: Parallel multi-block computational features (60x64x136 CV mesh divided into 6 blocks). Percentage of computational cost for each block and for the their interpolation schemes. Tank unloading phase at a mass flow rate of 0.1 kg/s. Total simulation time = 24 min. Total computational time = 16 hours.

calculation load.

The first of the properties mentioned above is the most relevant aspect to be analysed in the present problem. The influence of the number of blocks (into which the computational domain is split) on the number of outer iterations necessary to solve a time increment has been studied. In order to do this, the first discretisation has been considered (15x16x34 CV), solving 2 minutes of the unloading process (from minute two to minute four). It has been observed that the number of outer iterations does not increase dramatically. For the single block situation, about 6 outer iterations per time-step have been needed to compute an accurate enough solution with the convergence truncation criteria exposed in section 4.4.3. If four blocks are employed, the maximum number of iterations increase, at most, by 35%.

The good numerical performance of the algorithm can be attributed to the local phenomena of mixed convection that characterised these processes. Although the flow is incompressible, analysing the velocity field inside the tank, it can be observed that, as the mass flow rate of water enters the tank, it is rapidly stopped due its low temperature. The imposition of a mass flow rate at the outlet can benefit the algorithm's performance considerably.

Previous experience have shown that the efficient use of the algorithm depends only on the multi-block discretisation selected (i.e., the load balances). In a previous work [27] it has been observed that if all blocks have the same number of CVs, less computational work is assigned to the first and last blocks. This is because of the definition of solid CVs at the lateral walls of the tank (tank chassis and insulation), where mass and momentum fluxes do not require evaluation. For this reason, in this discretisation, the first and last block have more CVs than the inner blocks, which have the same number of CVs. In Fig. 4.5, the main computational features of the simulation are printed for the third discretisation with 6 blocks defined. The computational work to solve each block and the cost to apply the interpolation schemes are plotted. It is remarkable that, for each block, the interpolation load has been considerably lower than the calculation load. Moreover, the computational time required for each block has been approximately the same. On the other hand, this figure also gives an idea of the communication work carried out in the computation. As can be seen, it has been considerably lower than the computational load.

With reference to computational savings, it is important to take into account Eqn. (4.15). Due to the increase in the number of control volumes, ideal computational savings are limited by the following equation:

$$cs_f = (CV_1 \; N) / CV_N \tag{4.16}$$

In this situation (i.e., the third discretisation split into six blocks), the ideal savings factor (cs_f) is 5.32. Taking into account this ideal situation, and analysing Fig. 4.5, the computational savings obtained can be estimated to be about 5. Using six PCs of a *Beowulf cluster*, composed by standard PCs (AMD K7 CPU at 1900 MHz) with a conventional network (100 Mbits/s 3COM network card and a 3COM switch) running Debian Linux 2.1 (kernel version 2.7.2.3), the transient computation has been solved in approximately 16 hours. This is in contrast with the 80 or so hours that the resolution of this situation could take without the aid of the parallel algorithm.

4.5 Illustrative numerical results and comparison with experimental data

In any numerical research into heat transfer and fluid flow phenomena applied to the analysis of thermal equipment, there are two main concepts that must be assessed: the verification of the numerical solutions and the validation of the mathematical model ($V\&V$). This must be dealt with before any conclusions are made from the numerical results obtained.

The main point of verifying the numerical solutions is to guarantee that the numerical model solved corresponds to the solution of the mathematical model assumed. Discretisation errors produced in the conversion of the mathematical model to the algebraic equation systems should be estimated [28]. In the validation of the mathematical model, the appropriateness of the model that is assumed to reproduce "reality" should be verified. Details about the verification of the code and the numerical results have been commented in Chapter 3.

In this chapter, an *h-refinement* procedures have been performed in order to verify the numerical solutions. Numerical schemes have been fixed in order to analyse the influence of the mesh spacing and time increment on the numerical solutions obtained. Hereafter, the results of the verification and validation of the numerical results for each case considered are discussed.

4.5.1 Unloading phase case

As has been commented before, three computational meshes of 15x16x34, 30x32x68 and, 60x64x136 CVs have been considered. The simulation time has been discretised in time increments of 0.1, 1.0 and 10 seconds. To validate the mathematical model, the experimental data reported by [4], corresponding to the defined problem for an inlet mass flow rate of 0.1 kg/s has been used. Temperature measurements from three thermocouple stands arranged vertically inside the tank have been provided. Data has been available for a process lasting 24 minutes, with data acquire every 4 minutes. The accuracy of the temperature measurements has been considered to be within ±0.1 °C.

In order to analyse the influence of the temporal discretisation, the first mesh (15x16x34 CVs) has been solved for the three time increments commented above. While noticeable differences appeared when comparing the solutions with time-increments of 10 and 1 second, lesser discrepancies have been observed when analysing the 1 and 0.1 second increments.

The influence of mesh spacing has been analysed by fixing the temporal discretisation to one second. In Fig. 4.6, the numerical results are compared to the experimental data. The transient vertical temperature distribution at the centreline of the tank is plotted at six instants of the unloading process. Together with the experimental data, numerical results for the three meshes selected are presented.

A good agreement with the experimental data is observed. The higher the level of refinement, the better the experimental agreement. However, the highest level of discretisation employed could still be insufficient, specially during the first minutes of simulation. Considerable differences appear among the solutions obtained with the different meshes. Nevertheless, as the process goes on, the differences between the second and third meshes are reduced considerably.

From the numerical analysis performed in this section, the numerical solutions obtained using the third level of discretisation (i.e., 60x64x136 CV) and a time increment of one second, have been assumed to be accurate enough. In general, the comparisons presented show a convergence to an asymptotical solution as the discretisation parameters are refined.

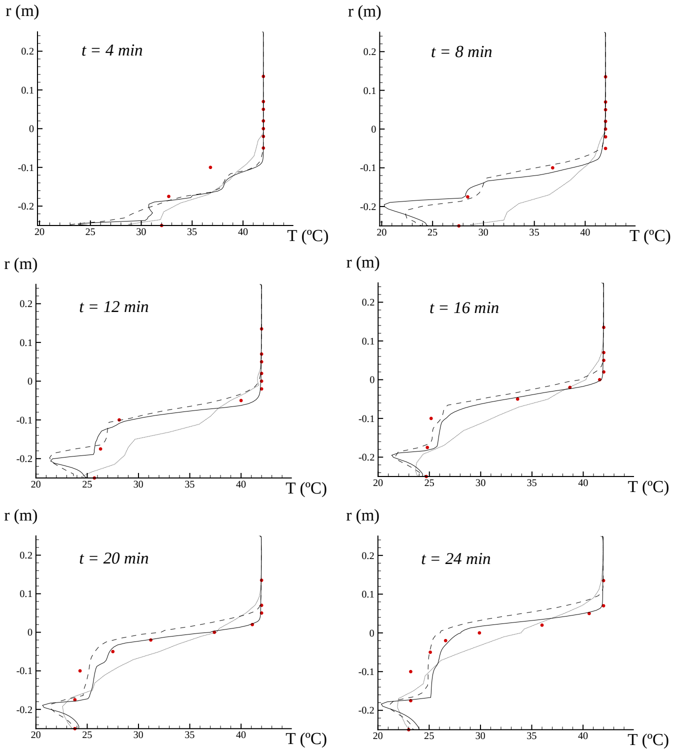

Figure 4.6: Computational results vs. experimental data. Transient vertical temperature distribution at the centreline of the tank. Dots, experimental data [4]; solid line, 60x64x136 CV mesh; dashed line, 30x32x68 CV mesh; dotted line, 15x16x34 CV mesh.

4.5.2 Loading phase case

The influence of the time discretisation has been analysed by solving the first 16 min of the load process with Test 1 (see Table 4.1) and comparing the numerical results obtained for the three different time increments. In this case, the first level of refinement (53x191) has been used. For increments considered, the vertical distribution of temperature at the mean distance between the center of the tank and the vertical wall at different instants are given in Fig. 4.7.

In general, there are no noticeable discrepancies between solutions obtained with the different time increments. However, for the largest Δt a higher number of itera-

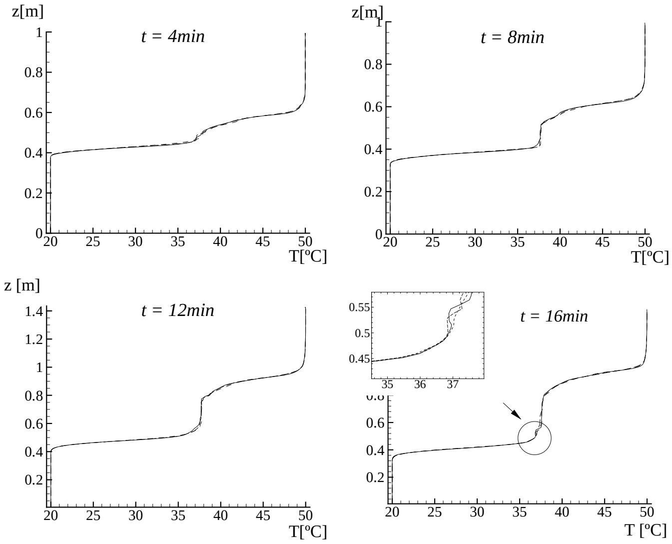

Figure 4.7: Computational results for different time discretisation. Transient vertical temperature distribution at the mean distance between the center of the tank and the vertical wall. solid line $\Delta t = 0.05s$; dashed line $\Delta t = 0.1s$; long dashed line $\Delta t = 1s$. Numerical results obtained for 53x191 CV mesh.

tions per time step to reach convergence has been required. Furthermore, the largest Δt has been also tested for the finnest meshes observing convergence instabilities as the mesh is refined.

Concerning to the mesh spacing, Test 1 has been solved for the three meshes considered and fixing the time step to 0.1 s. In Fig. 4.8 the transient vertical temperature distribution at the center of the tank is compared for the three levels of refinement. As the mesh is refined, the numerical solutions tends to an asymptotical value. Major discrepancies can be observed at the first instants, but as the time marches, differences are considerably reduced. Based on the numerical analysis performed, numerical solutions for the third level of refinement (174x458) with a time step of 0.1 s has been considered accurate enough to solve the problem.

Concerning the validation of the mathematical model, it has been shown that the hypothesis assumed for both situations (the unloading case and the loading phase), regarding its formulation, seems to be acceptable. The numerical solutions obtained are able to reproduce both processes of the tank properly. Nevertheless, it should be mentioned that, in some other physical situations involving heat transfer and fluid

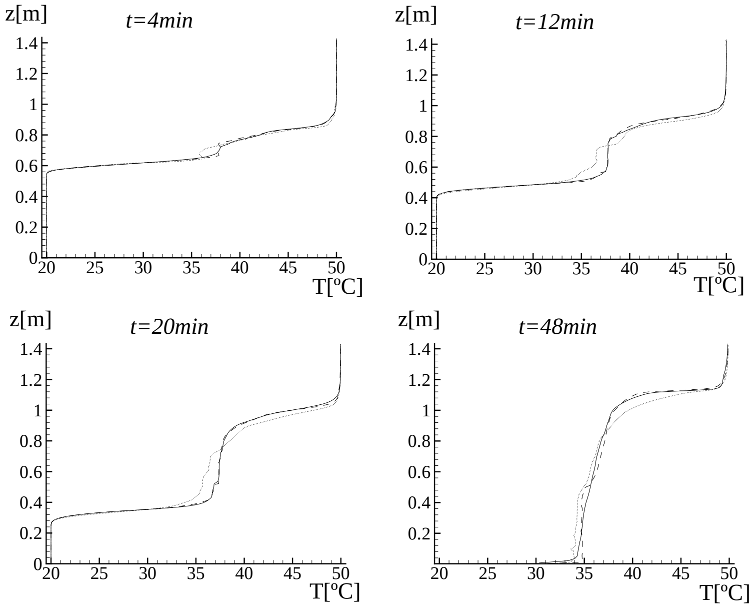

Figure 4.8: Computational results for different mesh discretisation. Transient vertical temperature distribution at the mean distance between the center of the tank and the vertical wall at different instants. solid line 174x458 mesh; dashed line 87x229 mesh; dotted line 53x191 mesh.

flow phenomena in storage tanks, the fluid flow can adopt a turbulent structure. In those cases, turbulence models should be considered in the numerical simulation [29, 30].

4.6 Thermal stratification analysis

In a transient three-dimensional numerical simulation, once the numerical solutions have been obtained, there is a considerable amount of data to be analysed. Qualitative results can be post-processed using commercial visualisation softwares. Thus, three-dimensional isocountours, two-dimensional sections or just xy-plots, can aid the designer to analyse the influence of the working conditions or design improvements on the optimum thermal behaviour of the storage equipment. However, in the optimisation process, quantitative measurements of the level of temperature stratifi-

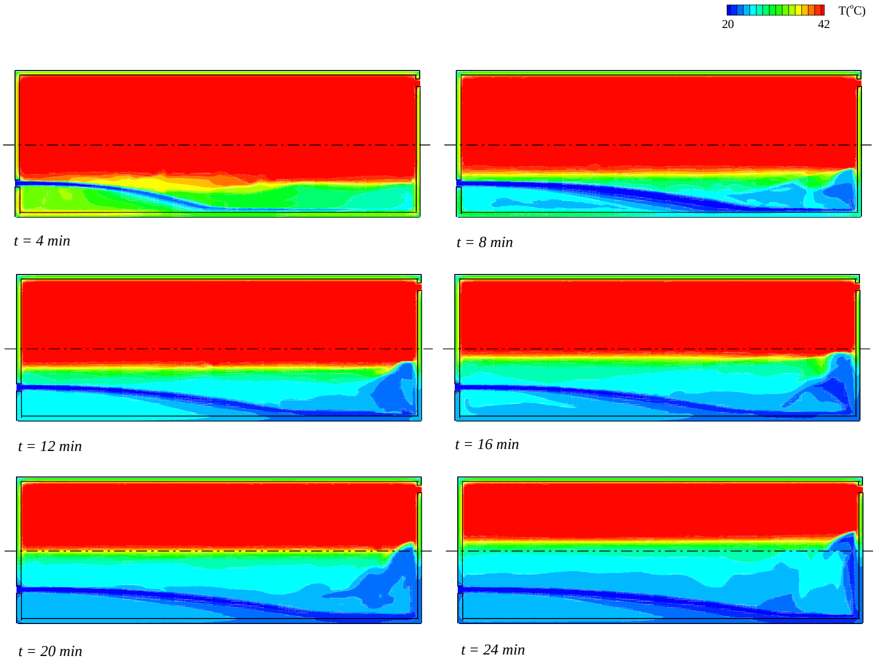

Figure 4.9: Computational results. Isotherms at different time instants and at the center plane of the tank. Mass flow rate of $\dot{m} = 0.1$ kg/s. 60x64x136 CV mesh.

cation appear to be an attractive tool for reporting possible improvements in a compact manner.

4.6.1 Unloading phase case

In addition to the plots shown in Fig. 4.6, illustrative results that describe the unloading process simulated are plotted in Figs. 4.9 and 4.10. In Fig. 4.9, isotherms at different time instants and at the center plane of the tank are presented for one of the mass flow rates analysed ($\dot{m} = 0.1$ kg/s). More detailed information is given in Fig. 4.10, where the transient radial temperature distribution at the center line of the tank for the mass flow rate of $\dot{m} = 0.025$ kg/s is plotted at different axial locations.

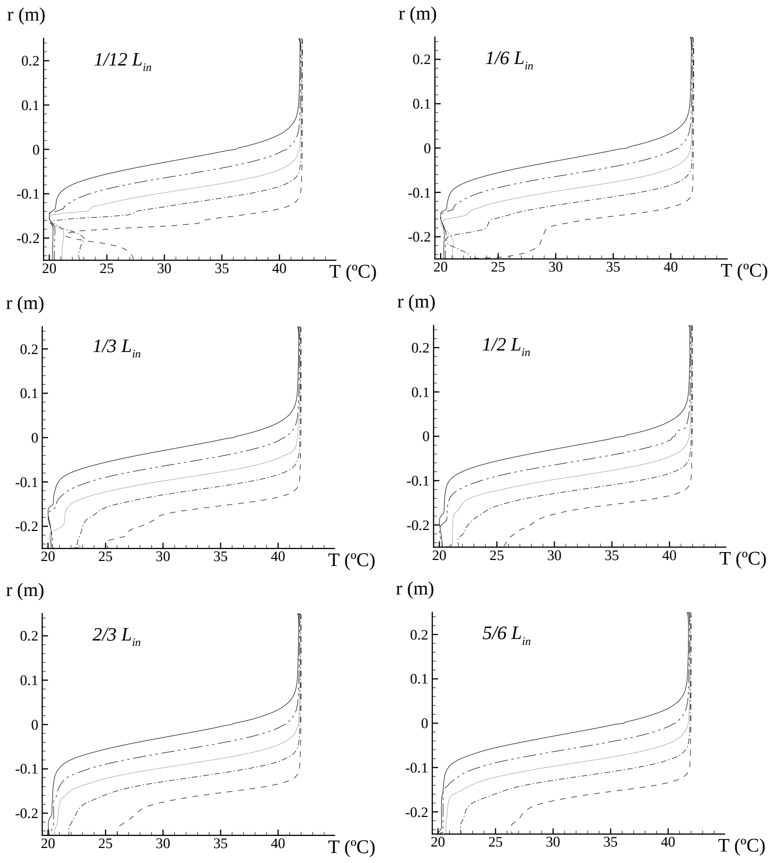

Figure 4.10: Computational results. Transient vertical distribution at tank different positions for a mass flow rate of $\dot{m} = 0.025$ kg/s. 60x64x136 CV mesh. Dashed line, $t = 20$ min; dash-dot line, $t = 40$ min; dotted line, $t = 60$ min; dash-dot-dot line, $t = 80$ min; solid line, $t = 100$ min.

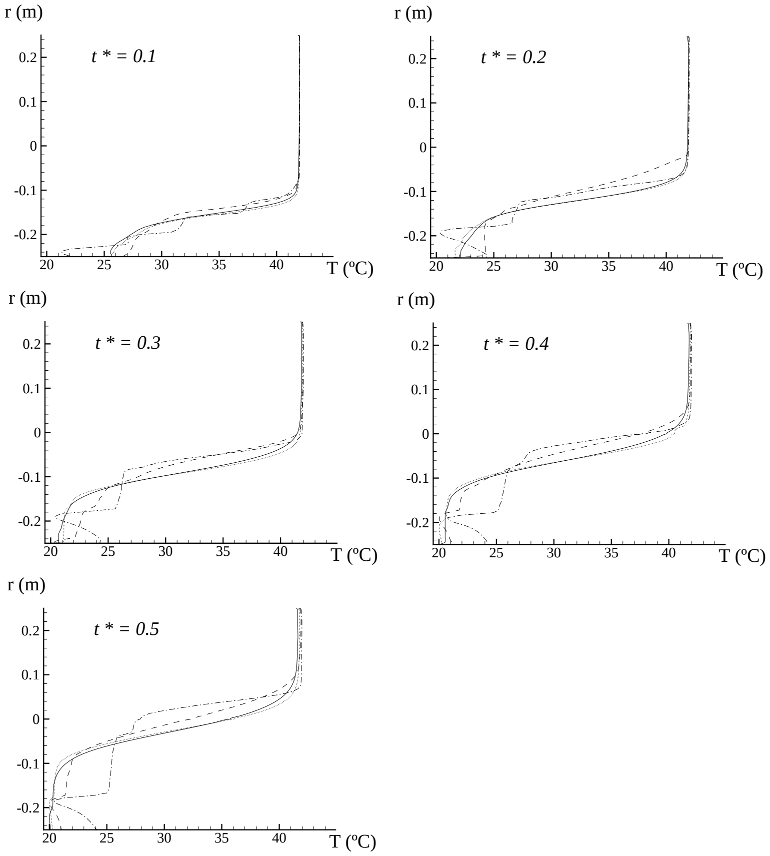

Figure 4.11: Computational results. Transient vertical temperature distribution at the center line of the tank for different mass flow rates. 60x64x136 CV mesh. Solid line, 0.0167 kg/s; dotted line, 0.025 kg/s; dashed line, 0.05 kg/s; dash-dot line, 0.1 kg/s.

The influence of the inlet mass flow rate on the level of temperature stratification inside the tank, and the estimation of this property by means of the parameters mentioned in section 4.2 is hereafter analysed.

The unloading process has been simulated considering four mass flow rates (0.0167, 0.025, 0.05 and 0.1 kg/s). The discretisation defined by the third level of refinement (i.e., 60x64x136 CV) and a time increment of one second have been used to perform the numerical simulations. All cases have been solved for an equivalent time of half a renovation of the tank. Taking the duration of a complete tank renovation as a reference ($t_{ref} = V\rho/\dot{m}$), numerical results are given for non-dimensional instants ($t^* = t/t_{ref}$) of: $t^* = 0.1, 0.2, 0.3, 0.4, 0.5$.

In Fig. 4.11, the transient vertical temperature distribution at the center line of the tank for the four mass flow rates studied is shown. As can be seen, for the three first mass flow rates (i.e., 0.0167, 0.025 and 0.05 kg/s) the tank is properly stratified as the process evolves. Please note that for the highest mass flow rate (0.1 kg/s), the temperature profile at the bottom of the tank differs considerably from the ideal situation. For $\dot{m} = 0.05$ kg/s, temperature distribution is slightly less stratified than it is for the smallest ones (0.0167 and 0.025 kg/s), while the temperature profiles for 0.025 and 0.0167 kg/s flow rates are quite similar.

In Table 4.5, the degree of thermal stratification is quantified by means of the evaluation of the *MIX* number, the non-dimensional exergy (ξ^*) of the tank and the non-dimensional thermocline thickness ($h_t^* = h_t/D$). As expected, the degradation of the stratification is considerably larger for the highest mass flow rate (0.1 kg/s). All stratification parameters are considerably higher than those observed for the other three cases (please note that, for an ideal stratified situation $MIX = 0$, $\xi^* = 0$ and $h_t^* = 0$).

	0.0167 kg/s			0.025 kg/s		
t^*	MIX	ξ^*	h_t^*	MIX	ξ^*	h_t^*
0.1	0.086	0.493	0.230	0.074	0.496	0.220
0.2	0.083	0.377	0.289	0.068	0.348	0.247
0.3	0.081	0.331	0.218	0.060	0.288	0.181
0.4	0.085	0.312	0.233	0.062	0.267	0.194
0.5	0.097	0.310	0.167	0.074	0.265	0.147
	0.05 kg/s			0.1 kg/s		
t^*	MIX	ξ^*	h_t^*	MIX	ξ^*	h_t^*
0.1	0.106	0.520	0.251	0.114	0.565	0.261
0.2	0.112	0.429	0.409	0.121	0.440	0.342
0.3	0.131	0.401	0.411	0.162	0.447	0.443
0.4	0.132	0.368	0.258	0.205	0.471	0.498
0.5	0.170	0.370	0.158	0.300	0.509	0.498

Table 4.5: Computational results. Non-dimensionless numbers at different instants for mass flow rates of: 0.0167, 0.025, 0.05 and 0.1 kg/s. 60x64x136 CV mesh.

With reference to the thermal stratification time evolution, it improves as it approaches the end of the experiment for all cases but the last one ($\dot{m} = 0.1$ kg/s). At the beginning, since the whole tank is warm, the entrance of the cold fluid provokes a sudden mixing between cold and warm fluid layers. As time progresses, the bottom of the tank is filled with a cold layer of fluid, and lower temperature differences are given between the bottom of the tank and the inlet fluid. Therefore, mixing due to the inlet mass flow rate decreases.

For the mass flow rate of $\dot{m} = 0.1$ kg/s, the cold stream enters the tank with a high momentum, causing a sudden mixing with the bottom fluid layer, as can be observed in Fig. 4.9. The best results have been obtained for the mass flow rate of 0.025 kg/s, even when mixing due to the inlet stream is expected to be lower for the smallest mass flow rate (0.0167 kg/s). In this case, the duration of the draw-off process induces an increase of mixing due to thermal diffusion inside the tank. These effects can be also observed in Fig. 4.11.

Sometimes, the measurement of the thermocline thickness at the middle of the tank (h_t^*) cannot provide a clear estimate of how the whole tank is stratified. Since the evolution of the temperature inside the tank is three-dimensional, multidimensional distributions of this parameter can help us to clarify its thermal behaviour. In Fig. 4.12, the variation of the thermocline thickness along the axial direction (z-direction) at the middle plane of the tank is plotted. As can be seen, specially during the first moments of simulation, considerable differences appear depending on the axial position under evaluation. The closer to the inlet zone the larger the thermocline thickness. However, as the process evolves, the axial distribution of the thermocline tends to be constant.

Although, for all situations, the *MIX* number estimates a good level of temperature stratification (values near to zero), the value of *MIX* tends to increase with time on average. This is due to the way the *MIX* factor is evaluated. Considering different stages of the unloading process, equivalent temperature stratifications (proportional deviations from the ideal situation) do not have the same *MIX* factor. In this sense, this value can help us to compare different situations at the same time instant, but it does not allow to analyse the evolution of the thermal stratification with time.

This limitation can be overcame by analysing the non-dimensional exergy of the tank. Since its evaluation is independent of the amount of energy stored in the tank, it allows a better estimation of the transient evolution of the level of temperature stratification. Observing Table 4.5, it can be seen that at the beginning, the non-dimensional exergy presents the largest values for all situations. Clearly, the most mixing takes place at that time. As the tank is progressively unloaded, its value tends to level out, as the rate of mixing at the inlet becomes considerably diminished.

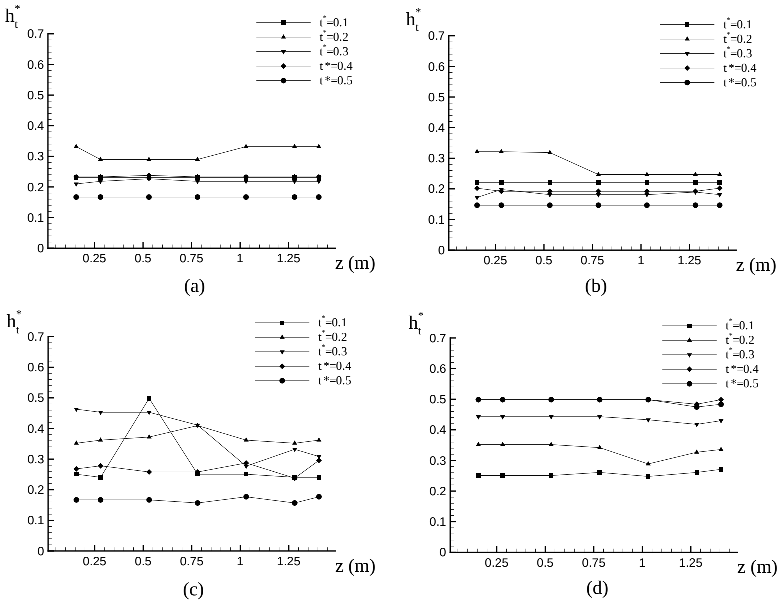

Figure 4.12: Computational results. Non-dimensional thermocline thickness for different tank sections at different instants. 60x64x136 CV mesh. (a) $\dot{m} = 0.0167$ kg/s, (b) $\dot{m} = 0.025$ kg/s, (c) $\dot{m} = 0.05$ kg/s, (d) $\dot{m} = 0.1$ kg/s.

4.6.2 Loading phase case

Three different inlet and initial conditions (described in section 4.3.2) during the loading phase of a storage tank have been analysed. The main objective has been to evaluate the behaviour of the manifold diffuser under different working conditions and at the same time to carry out quantitative measurements of the degree of stratification achieved with this device.

In Fig. 4.13 are plotted the vertical temperature distribution at different instants for each test analysed. Temperature profiles are given at the mean distance from the center of the tank and the tank wall. In addition, contours of the transient temperature evolution are plotted in Figs. 4.14, 4.15 and 4.16.

Test 1 (see Fig. 4.14) corresponds with a load process at a constant inlet temperature. As has been described in section 4.3.2, the fluid entering the tank is at a temperature between the top and bottom temperatures. Under these working conditions, the inlet stream exits at the manifold height corresponding with the most closest level of temperature for the fluid in the core. In this sense, the manifold not only reduces the momentum of the inlet stream but also directs the fluid to its corresponding temperature level. However, natural convection between hot and cold fluid layers inside the tank, provokes a flow recirculation through the manifold orifices located at the half upper part of the tank. These effects can also be observed in the figure, where the hot fluid at the top of the tank is entering through the manifold orifices reducing the hot water fluid layer at the top as the process evolves. This results in an enhancement of the mixing and the growth of the thermocline thickness (see Fig. 4.13 a). At the end of the test, more than 75% of the tank is filled with water at a moderate temperature (34 - $40°C$), while almost a 25% remains near the warmest temperature ($50°C$).

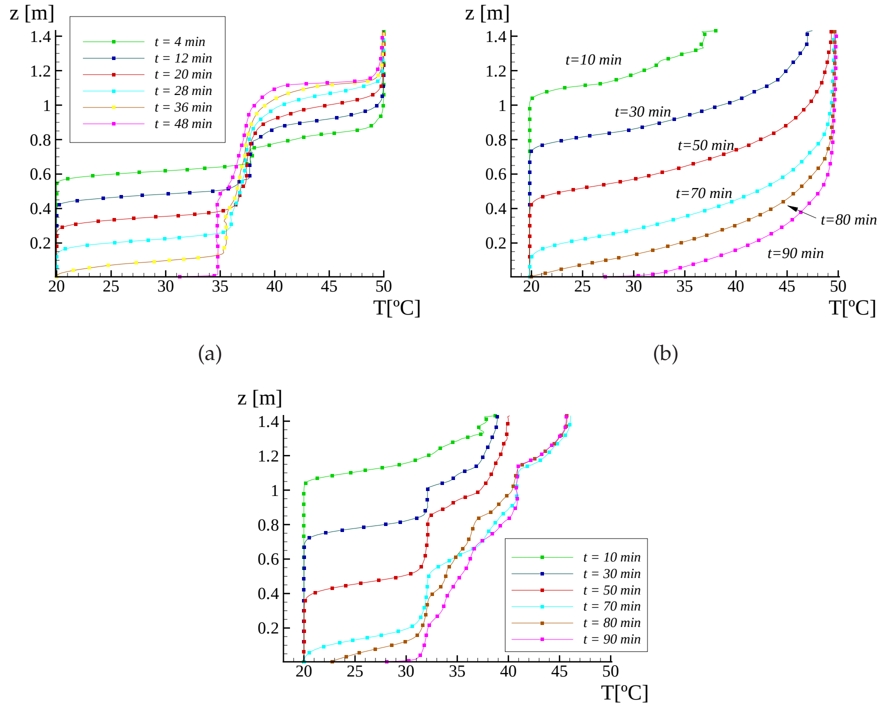

(a)

(b)

(c)

Figure 4.13: Computational results. Loading phase case. Transient vertical temperature evolution at the center line between the cylinder axis and the tank wall. (a) Test 1; (b) Test 2; (c) Test 3

In Test 2 (see Fig. 4.15), the tank initially at uniform cold temperature, is charged at a constant warm temperature. Ideally, the charging period duration is about 90 min, and at the end of the test the tank must be completely filled with water at the inlet temperature (for test conditions, $50°C$).

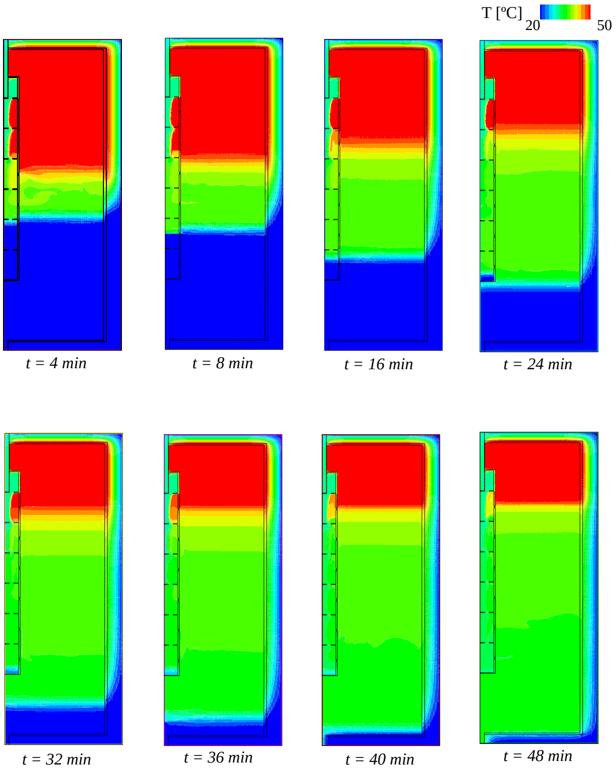

t = 4 min *t = 8 min* *t = 16 min* *t = 24 min*

t = 32 min *t = 36 min* *t = 40 min* *t = 48 min*

Figure 4.14: Computational results. Loading phase case. Transient temperature profiles for Test 1. 174x458 CVs mesh.

As in Test 1, the manifold reduces the momentum of the inlet stream and distributes the inlet fluid at its corresponding temperature level. During the first instants, the hot fluid exits the manifold at the highest possible location (see Fig. 4.15). However, as this position is at a certain distance from the top wall of the tank, a mixing between hot and cold fluid occurs in almost the 25% of the top volume of the tank. As the charging process continues, the thermocline region is developed, but its thickness has been conditioned by the initial mixing process. This has been also observed by Cònsul et al. [31]. In their work, they studied the effects of the position of the manifold in the thermocline thickness, and concluded, among other things, that during the charging process at constant temperature, the larger the inlet section of the manifold, the thicker the thermocline.

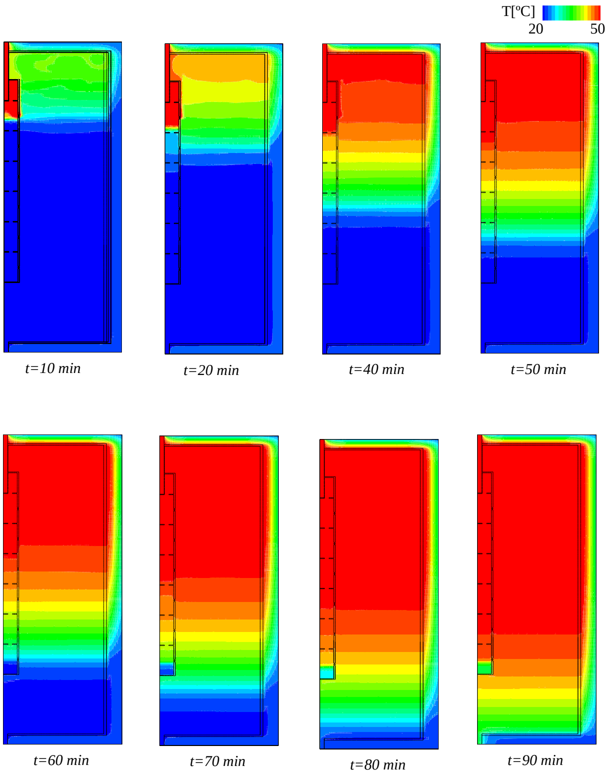

Figure 4.15: Computational results. Loading phase case. Transient temperature profiles for Test 2. 174x458 CVs mesh.

At the end of the theoretical charging process (the end of the test, see Fig. 4.15), the tank has not been fully-charged. This is mainly due to the mixing that occurs during the formation of the thermocline, as has been commented above. As can be observed in the figure, around a 35% of the tank is at a temperature between 30 - $45°C$.

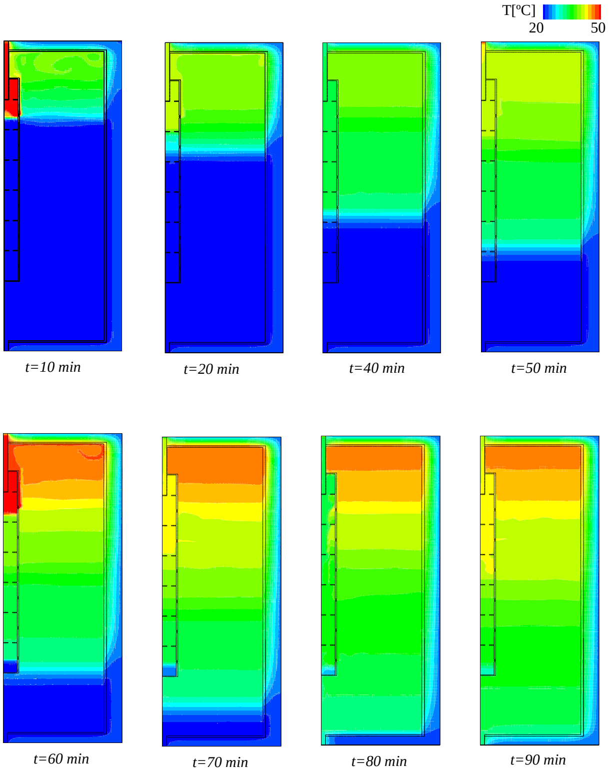

Figure 4.16: Computational results. Loading phase case. Transient temperature profiles for Test 3. 174x458 CVs mesh.

In Test 3, see Fig. 4.16, the inlet temperature varies with time. Then, the fluid enters the tank at different heights depending on its temperature. The recirculation effects through the manifold orifices due buoyancy forces has also been observed. However, as most of the time, temperature differences between the top and bottom of the tank are not as larger as in Test 2, the mixing is moderate. In spite of the adversely inlet conditions, at the end of the process the level of stratification achieved is acceptable.

In addition to the plots given, in Table 4.6, the level of stratification is quantified by means of the evaluation of the *MIX* number and the non-dimensional exergy (ξ^*). As can be observed, both non-dimensional parameters show the same trend. For Test 1, as has been commented before, a degradation of the stratification occurs as

Test 1					
t [min]	MIX	ξ^*	t [min]	MIX	ξ^*
4	0.066	0.172	28	0.178	0.264
8	0.077	0.193	32	0.201	0.273
12	0.093	0.21	36	0.223	0.277
16	0.110	0.227	40	0.241	0.288
20	0.132	0.243	44	0.257	0.296
24	0.155	0.255	48	0.271	0.316

Test 2			Test 3		
t [min]	MIX	ξ^*	t [min]	MIX	ξ^*
10	0.92	0.548	10	0.92	0.548
20	0.78	0.43	20	0.847	0.456
30	0.65	0.33	30	0.80	0.452
40	0.52	0.27	40	0.766	0.442
50	0.39	0.245	50	0.70	0.383
60	0.27	0.213	60	0.58	0.321
70	0.171	0.198	70	0.54	0.306
80	0.101	0.188	80	0.563	0.29
90	0.06	0.182	90	0.543	0.289

Table 4.6: Computational results. Loading process. Non-dimensional parameters at different instants for the three load tests. 174x458 CVs mesh

the process evolves. The mixing enhancement produced by buoyancy forces reduces gradually the hot fluid layer at the top of the tank, which is reflected in the increase of the non-dimensional exergy.

In Tests 2 and 3, the trend is to increase the level of stratification ($\xi^* \to 0$) once the sudden initial mixing has occurred. In Test 2, the development of the thermocline tends to level out the mix between hot and cold fluid layers. In this case, as more fluid is introduced, the thermocline region is pushed down leaving at the top, a region of uniform temperature and thus, decreasing the mixing at the inlet zone. With reference to Test 3, after the initial mixing, the difference between temperature of the fluid entering the tank and the fluid at the core is lower. This is reflected in a gradual reduction of the mixing phenomena. The evolution to a certain level of stratification at the end of this test, is quantitative reflected in the decreasing of the non-dimensional exergy.

Further comments

Analysing the results obtained for both situations studied, the charging and discharging of the storage, it is noticeable that in some situations non-dimensional exergy and *MIX* numbers do not show the same trend. This contradictory behaviour seems to be related with the fact that *MIX* number is referred to the energy content in the tank and, with the relative position of the thermocline in the tank (it seems to depend whether the thermocline is moving upwards or downwards the tank). As has been studied by Rosen [13], storage tanks with the same amount of energy stored, could have different level of stratification. Thus, energy-based analysis of stratification could fails in the quantitative measurement of the degree of stratification.

On the other hand, en exergy-based analysis is capable of quantifying the maximum potential associated with the incoming thermal energy. Energy losses to the environment and mixing due to inlet streams degradate the quality of the energy stored in a tank in the sense that it could not be useful at the temperature at which it has been input to the tank. In this kind of process, where energy analysis are not capable of identifying process inefficiencies, exergy-based analysis can provide a tool for evaluate the quality of the energy stored and thus, the quantification of the degradation of stratification in storage tanks.

4.7 Conclusions

In this chapter the performance of thermal storage tanks under charging and discharging phases has been studied. The methodology followed from the definition of the problem, the assumption of a mathematical model, its conversion into a numerical model, and the analysis of the numerical solutions obtained have been also shown. A particular emphasis has been given to the verification of the numerical solutions and the validation of the mathematical model.

For the unloading process, considering the geometry of the problem, the case for different mass flow rates has been solved using three-dimensional cylindrical meshes. In this case, taking into account the high computational cost to solve this domain, parallel multi-block techniques have been used. Taking advantage of "low cost" parallel computational infrastructures (Beowulf clusters), and the use of appropriate algorithms to be performed on these computers, the inherent computational cost of this kind of simulations can then be reduced considerably. In this chapter, the computational performance of an algorithm based on the multi-block method for the numerical simulation of storage tanks has been shown, pointing out the computational savings obtained for this kind of situations.

Different ways of quantify the degree of thermal stratification have been reviewed and a new exergy-based non-dimensional parameter has been proposed. The usefulness of this parameter has been discussed on the basis of comparisons with other parameters employed in the literature. This analysis has been carried out for both situations proposed (i.e. for the unloading and for the loading process of thermal storage tanks). According with the results, the non-dimensional exergy parameter proposed reflects in a quantitative manner the behaviour and performance of the stores. In this sense, this parameter, based on exergetic analyses can aid in thermal storage design, assessing the comparative value of different storages design. This is especially important due to in solar systems, energy stored is more useful if it can be recovered at the same temperature at which it has been stored. Thus, exergy-based analysis is an useful tool, providing a method for measure thermal performance in this kind of equipment.

Nomenclature

c_p	specific heat at constant pressure ($J/kg\ K$)	S	area (m^2)
D	tank internal diameter (m)	s	specific entropy ($J/kg\ K$)
h	specific enthalpy (J/kg)	T	temperature (K)
h_t	thermocline thickness (m)	T_c	cold temperature (K)
h_t^*	non-dimensional thermocline thickness	T_{env}	ambient temperature (K)
k	thermal conductivity ($W/m\ K$)	T_h	hot temperature (K)
H	tank length / height (m)	t	time (s)
M	energetic momentum ($J\ m$)	t^*	non-dimensional time
$\dot{m}$	mass flow rate (kg/s)	t_{ref}	reference time (s)
N	number of blocks	U	overall heat transfer coefficient (W/m^2K)
n	number of control volumes		

Greek letters:

β	thermal expansion coefficient (K^{-1})	ξ	specific exergy (J/kg)
Θ	non-dimensional temperature	ξ^*	non-dimensional exergy
μ	dynamic viscosity ($Pa\ s$)	Ω	volume (m^3)
Ξ	exergy (J)	ρ	density (kg/m^3)

Subscripts:

i	ith tank control volume
in	inlet conditions
mix	mixed tank
o	dead state
r	radial direction
st	stratified tank
z	axial direction
θ	azimuthal direction

References

[1] R. Cònsul, I. Rodríguez, C.D. Pérez-Segarra, and M. Soria. Virtual prototyping of storage tanks by means of three-dimensional CFD and heat transfer simulations. *Solar Energy*, 77(2):179–191, 2004.

[2] J.H. Davidson and D.A. Adams. Fabric stratification manifolds for solar water heating. *Journal of Solar Energy Engineering*, 116:130–136, 1994.

[3] A. Musser and W.P. Bahnfleth. Parametric study of charging inlet diffuser performance in stratified chilled water storage tanks with radial diffusers: Part 1-Model development and validation. *HVAC and Research*, 7(1):31–65, 2001.

[4] S. Alizadeh. An experimental and numerical study of thermal stratification in a horizontal cylindrical solar storage tank. *Solar Energy*, 66(6):409–421, 1999.

[5] W. P. Bahnflet and A. Musser. Thermal performance of a full-fcale stratified chilled water thermal storage tank. *ASHRAE Transactions*.

[6] A. Musser and W.P. Bahnfleth. Parametric study of charging inlet diffuser performance in stratified chilled water storage tanks with radial diffusers: Part 2-Dimensional analysis, parametric simulations and simplified model development. *HVAC and Research*, 7(1):51–65, 2001.

[7] J.H. Davidson, D.A. Adams, and J.A. Miller. A coefficient to characterize mixing in solar water storage tanks. *Journal of Solar Energy Engineering*, 116:94–99, 1994.

[8] D.E. Adams and J.H. Davidson. Tank stratification with a flexible minifold. In *Proceedings of the 1993 American Solar Energy Society Annual Conference*, pages 277–281, 1993.

[9] E.M. Kleinbach, W.A. Beckman, and S.A. Klein. Performance study of one-dimensional models for stratified thermal storage tanks. *Solar Energy*, 50(2):155–166, 1993.

[10] G. Rosengarten, G. Morrison, and M. Behnia. A second law spproach to characterising thermally stratified hot water storage with application to solar water heaters. *Journal of Solar Energy Engineering*, 121:194–200, 1999.

[11] M. A. Rosen. Second-law analysis. approaches and implications. *International Journal of Energy Research*, 23:415–429, 1999.

[12] M. A. Rosen. Second-law analysis of aquifer energy storage systems. *Energy – The International Journal*, 24:167–182, 1999.

[13] M. A. Rosen. The exergy of stratified thermal energy storages. *Solar Energy*, 71(3):173–185, 2001.

[14] R. J. Krane. A second law analysis of the optimum design and operation of thermal energy storage systems. *International Journal of Heat and Mass Transfer*, 30(1):43–57, 1987.

[15] M. A. Rosen, N. Pedinelli, and I. Dincer. Energy and exergy analisys of cold thermal storage systems. *International Journal of Energy Research*, 23:1029–1038, 1999.

[16] G. L. Morrison and C. M. Sapsford. Long term performance of thermosyphon solar water heaters. *Solar Energy*, 30(4):341–350, 1983.

[17] A Arbel and M Sokolov. Improving load matching characteristics of a thermosyphonic solar system by thermostatically controlled circulation. *Solar Energy*, 52(4):347–358, 1994.

[18] J.H. Davidson, W.T. Carlson, and W.S. Duff. Impact of component selection and operation on thermal ratings of drain-back solar water heaters. *Journal of Solar Energy Engineering*, 114:219–226, 1992.

[19] H.Y. Wong. *Heat Transfer for Engineers*. Longman, 1977.

[20] S.V. Patankar. *Numerical heat transfer and fluid flow*. Hemisphere Publishing Corporation, 1980.

[21] I. Rodríguez, R. Cònsul, J. Cadafalch, and A. Oliva. Numerical studies of thermosyphon solar heaters. In *Proceedings of the 3rd ISES Europe Solar Conference (EUROSUN 2000)*, pages 1–9, 2000.

[22] I. Rodríguez, R. Cònsul, and A. Oliva. Thermal optimisation of storage tanks by means of three-dimensional CFD simulations. In *Proceedings of the Forum International Sur les Energies Renouvelables*, volume II, pages 442–447, 2002.

[23] M. Soria. *Parallel multigrid algorithms for computational fluid dynamics and heat transfer*. PhD thesis, Universitat Politècnica de Catalunya, 2000.

[24] R. Cònsul, C.D. Pérez-Segarra, K. Claramunt, J. Cadafalch, and A. Oliva. Detailed numerical simulation of laminar flames by a parallel multiblock algorithm using loosely coupled computers. *Combustion Theory and Modelling*, 7(3):525–544, 2003.

[25] M. Costa, D. Faggembauu, M. Soria, and Farré C. Comparación y descripción de diferentes niveles de simulación numérica de la piel de un edificio concebida como elemento pasivo de diseño. In *Anales de Ingeniería Mecánica (Revista de la Asociación Española de Ingeniería Mecánica, Año 12)*, volume 3, pages 1634–1639, 2000.

[26] J. Cadafalch, A. Oliva, C.D. Pérez-Segarra, M. Costa, and J. Salom. Comparative study of conservative and non conservative interpolation schemes for the domain decomposition method on laminar incompressible flows. *Numerical Heat Transfer, Part B*, 35(1):65–84, 1999.

[27] R. Cònsul, I. Rodríguez, and A. Oliva. Three-dimensional simulation of storage tanks by a parallel multiblock algorithm using loosely coupled computers. In *Proceedings of the ISES Solar World Congress 2003*, 2003.

[28] AIAA Journal. Special section: credible computational fluid dynamics simulations. *AIAA Journal*, 36:665–764, 1998.

[29] C.D. Pérez-Segarra, A. Oliva, M. Costa, and F. Escanes. Numerical experiments in turbulent natural and mixed convection in internal flows. *International Journal for Numerical Methods for Heat and Fluid Flow*, 5(1):13–33, 1995.

[30] R. Cònsul, I. Rodríguez, J. Cadafalch, and A. Oliva. Simulación numérica de tanques de acumulación de energía térmica. In *Proceedings of the IX Congreso Ibérico de Energía Solar*, pages 405–414, 2000.

[31] R. Cònsul, I. Rodríguez, K. Claramunt, and A. Oliva. Thermal stratification improvements in thermal storage tanks: Numerical analysis of directed inlet mass flow rates strategies. In *Proceedings of the 5th ISES Europe Solar Conference (EUROSUN 2004)*, 2004.

Chapter 5

Parametric study of the transient natural convection inside storage tanks. Global models analyses

Abstract. In the present chapter, the transient cooling of a fluid initially at rest, inside a storage tank submitted to heat losses to the ambient is studied. In order to identify the relevant non-dimensional groups that define the transient natural convection phenomenom that occurs, a non-dimensional analysis is carried out. The long-term behaviour of the fluid is modeled by formulating a prediction model based on global balances. A parametric study by means of several multidimensional numerical simulations led to correlate the Nusselt number and the transient mean fluid temperature, to feed the global model proposed. Special attention is given to the appropriateness of the spatial and time discretisation adopted, the verification of the numerical solutions and the post-processing tasks in order to obtain the correlations. The most relevant particularities of the numerical model developed are also pointed out.

.

5.1 Introduction

The performance of a thermal energy storage tank is significantly affected by the natural convection and associated heat transfer during charging and dischanging phases as has been analysed in previous chapter, but also during its still phase, where the heat exchange with the surroundings is the main mechanism of fluid movement inside the store. Thus, an effective optimisation of these devices requires an extensive knowledge of the heat transfer mechanism between the fluid and the environment.

Due to its importance for many practical applications, the transient process of cooling (or heating) a fluid inside an enclosure under natural convection, has been widely treated in the literature. However, most of the studies conducted have been focused on rectangular enclosures with imposed vertical wall temperatures on steady state situations [1, 2, 3] or considering the transient response of the fluid [4, 5].

On the other hand, cylindrical geometries have received lesser attention. Among the earlier studies can be cited the work conducted by Hyun [6]. He studied the transient mechanism of heat-up a fluid inside a cylinder initially at rest, submitted to a linear temperature gradient at the side wall. Raithby and Hollands [7] in their review cited the experimental studies done by Evans and Stefany about the transient response of fluids inside vertical and horizontal enclosures following a step change in wall temperature. These authors correlated the empirical data obtained in the quasi-steady regime to a single expression of the Nusselt number as a function of the Rayleigh number. Cotter and Charles [8, 9], in two papers, studied the transient natural convection of crude oil in a large vertical cylinder, presenting results of the time dependence of the Nusselt number and fluid temperature for several oil viscosities and aspect ratios.

More recently, Lin and Armfield [10] studied the transient response of the fluid in a vertical cylinder after a step change in the temperature wall until the stratification stage is reached. After this study, these authors [11] analysed the long-term behaviour of the cooling process in a vertical cylinder with fixed walls temperatures. Oliveski et al. [12] investigated the cooling of a vertical storage tank considering both, the tank and the insulation material. They considered different aspect ratios, insulation thicknesses for two different tank volumes and correlated the Nusselt number to the aspect ratio, the mean fluid temperature and the overall heat transfer coefficient for each tank volume studied. Although these correlations can be very useful, it is difficult to extrapolate their results to other situations than those exposed in the work. The lack of a non-dimensional analysis together with the fact that the correlations proposed were written as a function of dimensional parameters limit the range of application of these correlations to the specific cases presented. Papanicolaou and Belessiotis [13] analysed numerically the natural convection in a vertical cylinder with an imposed constant heat flux in its lateral surface, comparing also their numerical results for the transient temperature in the core of the cylinder, with an analytical expression given in the literature.

Considering the importance of the still phase within the different working regimes of storage tanks and the scarce information about this phenomena, the present study attempts to investigate, by means of numerical CFD simulations, the transient natural convection inside a vertical storage tank submitted to heat losses to the environment. The behavior of the fluid has been characterised and a global model has been presented. In order to obtain the main coefficients needed for these kind of global models, a non-dimensional analysis has been performed. From this analysis, the relevant non-dimensional groups that define the problem have been identified. Scaling relations to correlate the heat transfer coefficient to the relevant parameters have been proposed. A parametric study has been carried out in order to adjust the results of the detailed numerical simulations to the heat transfer relations. This parametric study has allowed to cover a wide range of working conditions of storage tanks in solar domestic hot water systems.

5.2 Problem definition

In an attempt to investigate the transient phenomena that takes place during the cooling down of vertical hot water storage tanks used for solar domestic hot water systems, different tank parameters and working conditions have been studied. The solar storage tanks usually used in small domestic systems (i.e. collector areas up to 6 m^2, with tank volumes up to 0.4 m^3), are within the range of aspect ratios $H/D = 1.5 \div 3.5$.

The tank under study, has been made of $3mm$ of stainless steel wall and thermal insulation of fibber glass. An schematic of the vertical cylindrical storage tank is shown in Fig. 5.1. Different tank volumes $\Omega = 0.1 \div 0.4\, m^3$, with aspect ratios from $H/D = 1 \div 3.45$ and, insulation thickness varying within the range $\delta_{ins} = 0 \div 0.04$ m have been considered. These values cover most of the aspect ratios and insulation thicknesses used in commercial storage tanks.

The tank has experienced a cooling process due to a temperature gradient between the fluid and the ambient. Taking into account that the service water temperature in domestic hot water applications is around $60°C$, initial temperature of the tank, including solid walls and insulation material,has been considered in the range of $T_0 = 40 \div 70°C$. Ambient temperature has been fixed to $T_{env} = 20°C$ during the whole cooling process, while two different convection heat transfer coefficient between the external tank wall and the ambient have been considered: h_{ext}= 2 and

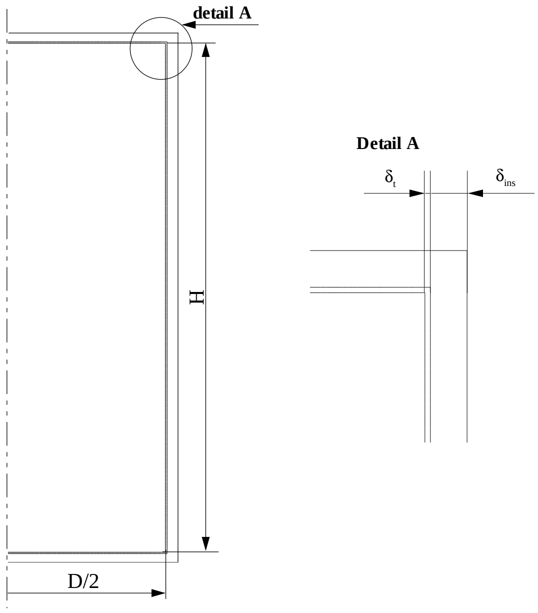

Figure 5.1: Problem definition. Schematic of the geometry of the storage tank under study.

$10\,W/m^2K$.

5.3 Global model analysis

The aim of the study is to characterise the transient behaviour of the fluid inside the storage tank, evaluating the long-term variation of its mean temperature and the heat losses to the environment. According with this objective and considering the problem defined in the previous section, a simplified mathematical model has been formulated. The following conditions and hypothesis have been considered:

- The tank has been modeled as divided into N layers of fluid

- Thermophysical properties have been taken constant and have been evaluated at the mean temperature between the ambient and initial fluid temperature

- One-dimensional heat losses (through the walls and the insulation) being modeled by an overall heat transfer coefficient between the inlet wall and the ambient ($\overline{U}$).
- The energy storage capacity of solid walls has been neglected

Taking into account the assumptions outlined, an energy balance for the k^{th} fluid layer of the tank can be formulated as:

$$\int_{\Omega_k} \rho c_p \frac{\partial \overline{T}_k}{\partial t} d\Omega + \int_{\partial\Omega_k} \rho c_p T_k \overrightarrow{v}\,\overrightarrow{n}\, dS = -\int_{\partial\Omega_k} \overrightarrow{q} \cdot d\overrightarrow{S} = -\dot{Q}^k_{loss} \tag{5.1}$$

The heat losses through the walls ($\dot{Q}^k_{loss}$) can also be expressed in terms of a superficial heat transfer coefficient between the wall and the fluid or in terms of the overall heat transfer coefficient between the wall and the ambient as:

$$\dot{Q}^k_{loss} = h_k(\overline{T}_k - \overline{T}_{wk})S_k = \overline{U}_k(\overline{T}_{wk} - T_{env})S_k \tag{5.2}$$

The system of equations that results from the above formulation can be solved if the values of the heat transfer coefficients (h_k) and the advective fluxes between the layers (second integral term in the left hand side of the balance) are known. These values can be obtained either from the literature, from experiments or by means of detailed numerical simulations. This question is addressed in further sections.

5.3.1 One-temperature level global model

The global energy balance presented (Eqn. 5.1) can be written considering only one-temperature level, i.e. $N = 1$. For this particular case, Eqn. 5.1 reads:

$$\rho c_p \frac{\partial \overline{T}}{\partial t}\Omega = -\int_{\partial\Omega} \overrightarrow{q} \cdot d\overrightarrow{S} = -\dot{Q}_{loss,B} - \dot{Q}_{loss,H} - \dot{Q}_{loss,T} \tag{5.3}$$

Equation 5.3 expresses that the transient variation of the mean temperature in the tank equals the energy losses through the top ($\dot{Q}_{loss,T}$), bottom ($\dot{Q}_{loss,B}$) and lateral ($\dot{Q}_{loss,H}$) walls. In a similar manner as Eqn. 5.2, these heat losses through the walls can be evaluated as:

$$\dot{Q}_{loss,B} = h_B(\overline{T} - \overline{T}_{wB})S_B = \overline{U}_B(\overline{T}_{wB} - T_{env})S_B \tag{5.4}$$

$$\dot{Q}_{loss,H} = h_H(\overline{T} - \overline{T}_{wH})S_H = \overline{U}_H(\overline{T}_{wH} - T_{env})S_H \tag{5.5}$$

$$\dot{Q}_{loss,T} = h_T(\overline{T} - \overline{T}_{wT})S_T = \overline{U}_T(\overline{T}_{wT} - T_{env})S_T \tag{5.6}$$

where $\overline{U}_H$, $\overline{U}_B$ and $\overline{U}_T$ are the overall heat transfer coefficients between the inner wall of the tank and the ambient for the vertical, bottom and top walls respectively. These coefficients can be calculated (referred to the inner wall) as:

$$\overline{U}_H = \left[\frac{0.5D}{k_t}\ln(\frac{r_t}{0.5D}) + \frac{0.5D}{k_{ins}}\ln(\frac{r_{ins}}{r_t}) + \frac{0.5D}{r_{ins}}\frac{1}{h_{extH}}\right]^{-1} \tag{5.7}$$

$$\overline{U}_B = \left[\frac{\delta_t}{k_t} + \frac{\delta_{ins}}{k_{ins}} + \frac{1}{h_{extB}}\right]^{-1} \tag{5.8}$$

$$\overline{U}_T = \left[\frac{\delta_t}{k_t} + \frac{\delta_{ins}}{k_{ins}} + \frac{1}{h_{extT}}\right]^{-1} \tag{5.9}$$

where r_t and r_{ins} are defined according with Fig. 5.1 as: $r_t = 0.5D + \delta_t$ and $r_{ins} = r_t + \delta_{ins}$.

Re-writting Eqns. 5.4 to 5.6 as a function of the mean fluid temperature and the ambient, and eliminating wall temperature:

$$\dot{Q}_{loss,B} = \frac{\overline{U}_B h_B}{\overline{U}_B + h_B}(\overline{T} - T_{env})S_B \tag{5.10}$$

$$\dot{Q}_{loss,H} = \frac{\overline{U}_H h_H}{\overline{U}_H + h_H}(\overline{T} - T_{env})S_H \tag{5.11}$$

$$\dot{Q}_{loss,T} = \frac{\overline{U}_T h_T}{\overline{U}_T + h_T}(\overline{T} - T_{env})S_T \tag{5.12}$$

Thus, Eqn. 5.2 finally reads:

$$\rho c_p \frac{\partial \bar{T}}{\partial t}\Omega = -\left(\frac{\overline{U}_B h_B S_B}{\overline{U}_B + h_B} + \frac{\overline{U}_H h_H S_H}{\overline{U}_H + h_H} + \frac{\overline{U}_T h_T S_T}{\overline{U}_T + h_T}\right)(\overline{T} - T_{env}) \tag{5.13}$$

If it is assumed that the external heat transfer coefficient (h_{ext}) is nearly the same for the top, bottom and lateral walls ($h_{extH} \approx h_{extB} \approx h_{extT} \approx h_{ext}$), the values of the overall heat transfer coefficient will also be nearly the same ($\overline{U}_T = \overline{U}_B \approx \overline{U}_H = \overline{U}$), then using an unique superficial heat transfer coefficient to characterise heat losses through the walls (h), Eqn. 5.13 reduces to:

$$\rho c_p \frac{\partial \bar{T}}{\partial t}\Omega = -\left(\frac{\overline{U} h S}{\overline{U} + h}\right)(\overline{T} - T_{env}) \tag{5.14}$$

The above equation can be easily integrated, mathematical o numerically, if the value of the transient heat loss coefficient ($h = f(t)$) is known.

5.4 Detailed numerical experiments for the global model

The global model presented in previous section is quite simple and easy to solve. The main problem of these kind of global models is the lack of empirical data (or correlations) about the transient heat transfer coefficients to feed them properly. In this section, in order to find the information needed to feed-back the model, a parametric study of the problem has been carried out. As a first step, the non-dimensional groups that define the case have been identified by means of a non-dimensional analysis of the situation presented. After that, the results of the several detailed numerical simulations of the thermal and fluid dynamic behaviour of the storage tank have been adjusted to find the heat transfer relations.

5.4.1 Non-dimensional analysis

The governing equations presented in section 2.2 have been non-dimensionalised by substituting:

$$\overrightarrow{r} = \overrightarrow{r}^*\, L_{ref}; \quad \overrightarrow{v} = \overrightarrow{v}^*\, v_{ref}; \quad T = T_{env} + \Theta\Delta T_{ref};$$

$$p = \rho v_{ref}^2 p^*; \qquad t = \frac{\tau L_{ref}}{v_{ref}}$$

where the characteristic dimension of the body, reference velocity and temperature have been assumed as:

$$L_{ref} = H; \qquad v_{ref} = \frac{\alpha}{L_{ref}};$$

$$\Delta T_{ref} = T_0 - T_{env}; \quad T_{ref} = \frac{(T_0 + T_{env})}{2.0}$$

Thus, governing equations in their non-dimensional form can be written as:

$$\nabla \cdot \overrightarrow{v}^* = 0 \tag{5.15}$$

$$\frac{D\overrightarrow{v}^*}{D\tau} = -\nabla p^* + Pr\,\nabla^2\overrightarrow{v}^* - Ra\,Pr\Theta \tag{5.16}$$

$$\frac{D\Theta}{D\tau} = \nabla^2\Theta \tag{5.17}$$

From the definition of the problem described in section 5.2, heat transfer between the tank and the ambient has been defined by a given superficial heat transfer coefficient between the walls and the ambient (h_{ext}) and a constant ambient temperature

(T_{env}). Taking into account the symmetry of geometry and boundary conditions, the domain has been assumed axisymmetric. For this situation, the non-dimensional initial and boundary conditions have been defined as follows:

$$\begin{aligned}
\overrightarrow{v}^* = 0\,, \Theta = \Theta_0 \quad & \text{at} \quad (\tau = 0\,, r^*\,, z^*) \\
v_r^* = 0\,, \frac{\partial v_z^*}{\partial r^*} = 0\,, \frac{\partial \Theta}{\partial r^*} = 0 \quad & \text{at} \quad (\tau > 0\,, r^* = 0\,, z^*) \\
-\frac{\partial \Theta}{\partial r^*} = \frac{h_e H}{k_{ins}} \Theta \quad & \text{at} \quad (\tau > 0\,, r^* = \frac{D/2 + \delta_t + \delta_{ins}}{H}\,, z^*) \\
-\frac{\partial \Theta}{\partial z^*} = \frac{h_e H}{k_{ins}} \Theta \quad & \text{at} \quad (\tau > 0\,, r^*\,, z^* = 0\,, z^* = 1 + \frac{2.0(\delta_t + \delta_t)}{H})
\end{aligned} \tag{5.18}$$

With the aim of identifying the relevant non-dimensional groups that govern the behaviour of the fluid, the heat transfer through the walls and insulation has been assumed one dimensional and normal to the wall surfaces, neglecting the heat transfer in the other directions. Writing the boundary conditions only for the fluid domain:

$$\begin{aligned}
\overrightarrow{v}^* = 0\,, -\frac{\partial \Theta}{\partial r^*} = \frac{\overline{U_H} H}{k}(\Theta + \frac{1}{2}) \quad & \text{at } (r^* = \frac{D}{2H}\,, z^*) \\
\overrightarrow{v}^* = 0\,, -\frac{\partial \Theta}{\partial z^*} = \frac{\overline{U_B} H}{k}(\Theta + \frac{1}{2}) \quad & \text{at } (r^*\,, z^* = \frac{\delta_t + \delta_{ins}}{H}) \\
\overrightarrow{v}^* = 0\,, -\frac{\partial \Theta}{\partial z^*} = \frac{\overline{U_T} H}{k}(\Theta + \frac{1}{2}) \quad & \text{at } (r^*\,, z^* = 1 + \frac{\delta_t + \delta_{ins}}{H})
\end{aligned} \tag{5.19}$$

From the boundary conditions in non-dimensional form appears the aspect ratio (H/D) and a dimensionless group referred to the overall heat transfer coefficients at each wall:

$$\widehat{U}_H = \overline{U}_H H/k \qquad \widehat{U}_B = \overline{U}_B H/k \qquad \widehat{U}_H = \overline{U}_T H/k \tag{5.20}$$

Then, considering governing equations and boundary conditions for the problem analysed, the fluid temperature inside the store depends on the following non-dimensional groups:

$$\Theta = f(\overrightarrow{r}^*, \tau, Ra, \widehat{U}_H, \widehat{U}_B, \widehat{U}_T, H/D, Pr) \tag{5.21}$$

The Nusselt number

Heat losses through bottom, lateral and top tank walls can be evaluated as:

$$\dot{Q}_{loss,\,B} = \int\limits_{\partial\Omega_B} k\left(\frac{\partial T}{\partial z}\right)_{r,z=\delta_t+\delta_{ins}} dS \tag{5.22}$$

$$\dot{Q}_{loss,\,H} = -\int\limits_{\partial\Omega_H} k\left(\frac{\partial T}{\partial r}\right)_{r=D/2,z} dS \tag{5.23}$$

$$\dot{Q}_{loss,\,T} = -\int\limits_{\partial\Omega_T} k\left(\frac{\partial T}{\partial z}\right)_{r,z=\delta_t+\delta_{ins}+H} dS \tag{5.24}$$

or in terms of an average heat transfer coefficient, as has been defined by Eqn. 5.2.

Combining the above expressions and using non-dimensional variables, the dimensionless heat transfer coefficient at each wall, i.e. the Nusselt number, can be defined as:

$$\overline{Nu}_B = \frac{h_B H}{k} = \frac{1}{(\overline{\Theta}_B - \overline{\Theta}_{wB})S}\int\limits_{\partial\Omega_B}\left(\frac{\partial\Theta}{\partial z^*}\right)_B dS \tag{5.25}$$

$$\overline{Nu}_H = \frac{h_H H}{k} = \frac{1}{(\overline{\Theta}_H - \overline{\Theta}_{wH})S}\int\limits_{\partial\Omega_H}\left(\frac{\partial\Theta}{\partial r^*}\right)_H dS \tag{5.26}$$

$$\overline{Nu}_T = \frac{h_T H}{k} = \frac{1}{(\overline{\Theta}_T - \overline{\Theta}_{wT})S}\int\limits_{\partial\Omega_T}\left(\frac{\partial\Theta}{\partial z^*}\right)_T dS \tag{5.27}$$

The Nusselt number is a function of the non-dimensional fluid and wall temperatures. Thus, considering the above analysis and the dependence of the temperature with the relevant non-dimensional groups identified, in a general sense, the Nusselt number can also be expressed as a function of those parameters as:

$$\overline{Nu} = f(\tau, Ra, \widehat{U}_H, \widehat{U}_B, \widehat{U}_T, H/D, Pr) \tag{5.28}$$

or if it is assumed that the overall heat transfer at each walls is nearly the same, i.e. $\overline{U}_T = \overline{U}_B \approx \overline{U}_H = \overline{U}$:

$$\overline{Nu} = f(\tau, Ra, \widehat{U}, H/D, Pr) \tag{5.29}$$

5.4.2 Parametric study

In order to find the proper correlations between the heat transfer coefficient and temperature with the relevant non-dimensional groups that characterise the problem, a parametric study has been carried out by means of the resolution of detailed numerical CFD simulations.

The study has accounted for the variation of the different relevant non-dimensional groups, i.e. Ra, H/D, $\widehat{U}$. As governing equations have been solved in dimensional form, these parameters have been defined from the dimensional problem parameters (the insulation thickness δ_{ins}, the initial fluid temperature T_0, the ambient temperature T_{env}, the tank volume Ω, etc.). Therefore, values for each parameter have been considered within the ranges defined in section 5.2. Four different values for the aspect ratio $H/D = 1,\ 2,\ 3,\ 3.45$; six values for the initial temperature $T_0 = 40, 50, 55, 60, 65, 70\ {}^{\circ}C$; four for the insulation thickness $\delta_{ins} = 0, 0.01, 0.02, 0.04$ m; four for the tank volume $\Omega = 0.1,\ 0.2,\ 0.3,\ 0.4\ m^3$ and two for the external heat transfer coefficient $h_{ext} = 2,\ 10\ W/m^2K$ have been used. Ambient temperature in all situations has been set to $T_{env} = 20^{\circ}C$. These account for $Ra = 4.8 \cdot 10^{11}\ \div\ 10^{13}$, $H/D = 1\ \div\ 3.45$ and $\widehat{U} = 0.78\ \div\ 26.6$.

Taking into account that the total amount of cases considered for the parametric study equals 768, and that in terms of computational effort the resolution of the transient cooling process of all cases could be very costly, a further selection has been performed. First, for a fixed tank volume $\Omega = 0.3\ m^3$ and initial temperature $T_0 = 60^{\circ}C$, all other situations have been considered (i.e. a total of 32 cases considering four aspect ratios, four insulation thickness and two external heat transfer). After that, for the aspect ratio of $H/D = 3.45$, initial temperature of $T_0 = 60^{\circ}C$ and insulation thickness of $\delta_{ins} = 0.01$ m, four tank volumes have been considered. Then, fixing the insulation thickness to $\delta_{ins} = 0.02\ m$, the tank volume $\Omega = 0.3\ m^3$ and the external heat transfer coefficient $h_{ext} = 10\ W/m^2K$, seven initial temperatures have been investigated. This have resulted in a total number of 42 situations for the transient numerical simulation of the cooling process of the tank.

5.4.3 Numerical approach

Methodology

The detailed numerical experiments commented before have been carried out by applying the techniques described in Chapter 2. In other words, the governing equations together with the boundary conditions (Eqn. 5.18) in their dimensional form, have been integrated over the whole domain (fluid, solid walls and insulation material) by means of finite-volume techniques with fully implicit temporal differentiation, using cylindrical staggered grids. Diffusive terms have been evaluated using a second order central differences scheme, while convective terms have been approximated by means of the SMART scheme [14] using a deferred correction approach.

As the time needed to cool down the fluid inside the storage, i.e. to reach the ambient temperature, is theoretically infinite, a criteria to stop the transient simulation has been imposed. Aiming a general criteria for all situations considered, this criteria has been determined as a function of the non-dimensional mean temperature of the fluid. Considering the thermophysical properties constant, the mean fluid temperature can be defined as:

$$\overline{\Theta}(t) = \frac{1}{\Omega}\int\limits_{\Omega} \Theta d\Omega \tag{5.30}$$

Thus, the criteria to stop the transient simulation has been taken as the time the fluid requires to reach a temperature of $\bar{\Theta} <= 0.10$. On the other hand, for each time step, the iterative procedure has been truncated once the non-dimensional variables increments and residuals have been lower than 10^{-5} and once the relative increments of the computed mean Nusselt number has been below $10^{-7}\%$.

As has been commented before, due to the symmetry of the situation presented in 5.2, the computational domain selected is axisymmetric. To verify this hypothesis, one of the cases has been analysed considering fully 3D behaviour. The parameters corresponding with the case selected have been: $T_0 = 60°C$; $V = 0.3m^3$; $\delta_{ins} = 0m$; $H/D = 2$ ($H/D = 2$; $Ra = 2.38 \cdot 10^{12}$; $\widehat{U} = 18.456$). The meshes selected to solve both approaches (axisymmetric and fully 3D) have been of 72x144 and 72x40x144 CVs respectively. Taking into account the computational cost for solving the three-dimensional situation, the domain considered is half-cylinder instead of the whole cylinder. To do so, a symmetry boundary condition at the cylinder axial middle plane has been imposed. An example of both computational domains are shown in Fig. 5.2.

In Table 5.1 the results for the mean Nusselt number, $\overline{Nu}$, average internal wall temperature, T_w, and fluid temperature, $\overline{T}$, are given at different instants of the cooling process up to $t = 1800s$. Taking into account that the results obtained for axisym-

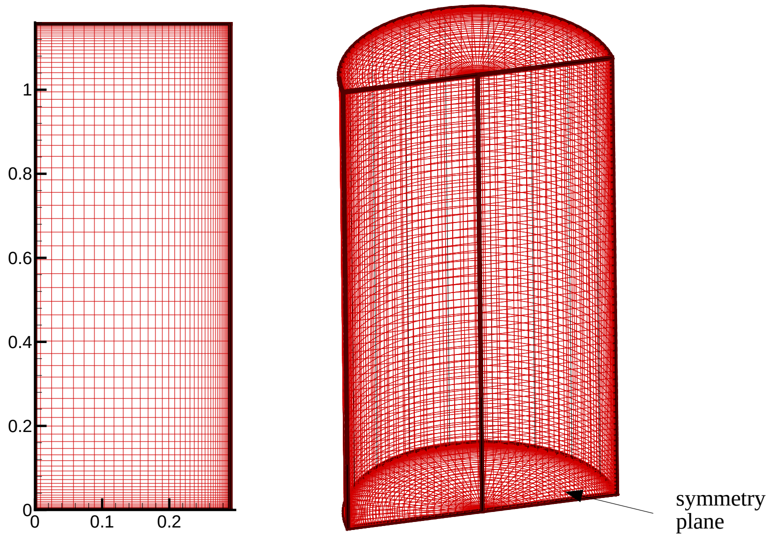

(a) (b)

Figure 5.2: Definition of the case. Example of the computational meshes. (a) axisymmetric domain (72x144 CVs), (b) Half-computational domain, three-dimensional mesh (72x40x144 CVs)

metric and fully 3D resolution agree quite well, the hypothesis of the axisymmetric domain has been assumed for all cases.

Verification

Numerical solutions presented have been obtained adopting an *h-refinement* criteria. Fixing numerical schemes, verification of the results account for the influence of the mesh spacing and the time increment on these numerical results. The parametric study carried out in the present work accounts for a determined number of computations. The post-processing verification presented here compresses four of these computations, one for each aspect ratio considered. These cases have been considered representative of all the others. The main parameters of each of these cases are given in Table 5.2. Notice that together with the non-dimensional relevant groups, the dimensional parameters (insulation thickness, tank volume, initial temperature, external heat transfer coefficient) are also given. These verification cases are hereafter

	$t = 300$ s			$t = 600$ s		
	axisymmetric	$3D$	$\%\epsilon$ [%]	axisymmetric	$3D$	$\%\epsilon$ [%]
$\overline{T}$	59.805	59.807	$3.34 \cdot 10^{-3}$	59.570	59.571	$1.68 \cdot 10^{-3}$
$\overline{T_w}$	57.970	57.911	$1.02 \cdot 10^{-1}$	57.690	57.664	$4.35 \cdot 10^{-2}$
$\overline{Nu}$	366.361	367.250	$2.42 \cdot 10^{-1}$	358.256	357.245	$2.82 \cdot 10^{-1}$
	$t = 900$ s			$t = 1200$ s		
	axisymmetric	$3D$	$\%\epsilon$ [%]	axisymmetric	$3D$	$\%\epsilon$ [%]
$\overline{T}$	59.338	59.338	$1.22 \cdot 10^{-6}$	59.106	59.107	$1.69 \cdot 10^{-3}$
$\overline{T_w}$	57.380	57.371	$1.57 \cdot 10^{-2}$	57.117	57.091	$4.55 \cdot 10^{-2}$
$\overline{Nu}$	348.909	347.120	$5.15 \cdot 10^{-1}$	336.282	335.429	$2.54 \cdot 10^{-1}$
	$t = 1500$ s			$t = 1800$ s		
	axisymmetric	$3D$	$\%\epsilon$ [%]	axisymmetric	$3D$	$\%\epsilon$ [%]
$\overline{T}$	58.876	58.877	$1.70 \cdot 10^{-6}$	58.647	58.649	$3.41 \cdot 10^{-3}$
$\overline{T_w}$	56.847	56.830	$2.99 \cdot 10^{-2}$	56.604	56.579	$4.42 \cdot 10^{-2}$
$\overline{Nu}$	325.241	326.128	$2.77 \cdot 10^{-1}$	319.147	319.688	$1.69 \cdot 10^{-1}$

Table 5.1: Comparison between axisymmetric and three-dimensional meshes at different time instants

denoted as *case v1*, *case v2*, *case v3* and *case v4*.

According to the preliminary results, considering the fluid structure and with the objective of describing the boundary layer near the walls (where the temperature and velocity gradients are the largest), it has been necessary to concentrate the mesh at the interface between the fluid and the solid wall by means of a tanh-like distribution [15]. The computational domain for the fluid has been discretised into non-uniform meshes of n_rxn_z CVs with a concentration factor of 2 in the zones near the interface between liquid and solid (i.e. near the tank walls), while for the solid domain (tank wall and insulation material) regular meshes have been used (see Fig. 5.2(a)).

case	H/D [-]	Ra [-]	$\widehat{U}$ [-]	T_0 $[^\circ C]$	h_{ext} $[W/m^2K]$	δ_{ins} [m]	Ω $[m^3]$
v1	1	$7.132 \cdot 10^{11}$	11.594	60	10	0.02	0.3
v2	2	$2.394 \cdot 10^{12}$	5.178	60	10	0.01	0.3
v3	3	$5.387 \cdot 10^{12}$	6.824	60	10	0	0.3
v4	3.45	$7.142 \cdot 10^{12}$	3.594	60	2	0.01	0.3

Table 5.2: Definition of the relevant parameters for the verification process

	H/D	
	1	2
m_1	(23+1+2)x(23+1+2)	(18+1+2)x(36+1+2)
m_2	(46+2+4)x(46+2+4)	(36+2+4)x(72+2+4)
m_3	(92+4+8)x(92+4+8)	(72+4+8)x(144+4+8)
m_4	(184+8+16)x(184+8+16)	(144+8+16)x(288+8+16)
	H/D	
	3	3.45
m_1	(16+1+2)x(48+1+2)	(15+1+2)x(53+1+2)
m_2	(32+2+4)x(96+2+4)	(30+2+4)x(105+2+4)
m_3	(64+4+8)x(192+4+8)	(60+4+8)x(210+4+8)
m_4	(128+8+16)x(384+8+16)	(120+8+16)x(420+8+16)

Table 5.3: Number of CVs in the h-refinement procedure for each aspect ratio including the fluid and solid walls n_rxn_z=$(n_f + n_t + n_{ins})$x$(n_f + n_t + n_{ins})$

For each of these computations, the mesh has been refined using 4 levels on the *h-refinement* criteria with a ratio of 2 (in each computational level, denoted with letter 'm', the mesh has been doubled, see Table 5.3). The criteria of refinement adopted, considers independently the fluid and the solid domains as it is shown in the table. Moreover, the simulation time has also been discretised in time steps of 0.25, 0.5, 1.0 and 2.0 s.

Concerning to the temporal discretisation, it has been selected *case v2* for the third level of spacial discretisation according with Table 5.3. The case has been solved up to 7200 s using the different time steps indicated above. For time steps of $\Delta t = 1s$ and $\Delta t = 2s$ convergence has been reached after a high number of outer iterations. During the first instants of the cooling process (up to $900s$), the iterative process has required more than 200 iterations for $\Delta t = 1s$. Furthermore, for the highest time step ($\Delta t = 2s$) the convergence has been totally unstable and in most time steps the convergence criteria has not been attained after 300 iterations (!). Although this number decreases with the development of the fluid stratification, still has required more than 50 iterations to achieve convergence criteria imposed at each time step. For the smallest Δt, the number of outer iterations required has been always below 20 even for the first instants, being around 8 and 12 for $\Delta t = 0.25s$ and $\Delta t = 0.5s$, respectively. For the smallest time steps, discrepancies between solutions obtained have not been noticeable. As the time to cool down the storage could be very large, depending of the situation under study, a high number of time steps to solve it is required. Considering the total number of time steps to be solved and the number of

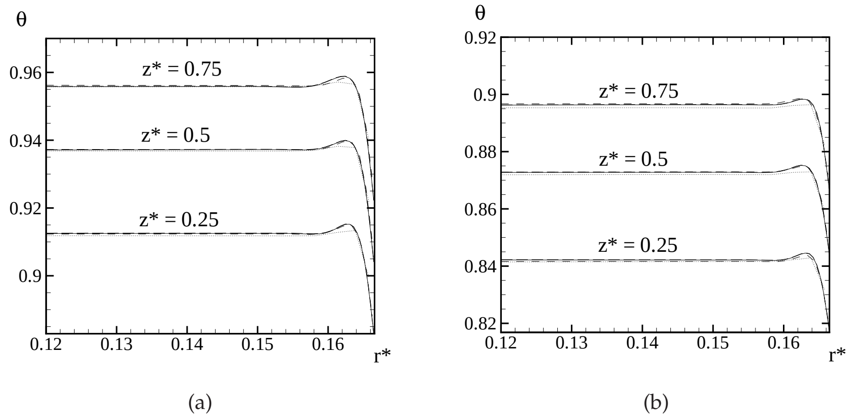

(a)

(b)

Figure 5.3: Verification. Fluid temperature profiles in the boundary layer at different heights with different levels of refinement for the verification *case v3*: dotted line (m1) , dash-dotted line (m2), dashed line (m3), and solid line (m4) (a) at 3600 s and (b) at 7200 s

outer iterations per each one needed to reach convergence, a temporal discretisation of $\Delta t = 0.5s$ has been adopted.

The influence of the mesh spacing has been analysed by fixing the time step to $\Delta t = 0.5s$. Then, simulations have been performed following the *h-refinement* criteria on the four cases selected. These cases have been solved up to 7200 s.

In Fig. 5.3 the temperature profiles near the boundary layer obtained with the different levels of refinement at selected tank heights and two time increments for the *case v3* are shown. As can be seen, there is no noticeable differences between levels of refinement m_3 and m_4. In Tables 5.4 and 5.5, a comparison between the different levels of refinement for the average Nusselt number, mean fluid temperature and solid wall interface temperature at different instants are given. The cases illustrated in the tables corresponds with *case v2* and *case v4*, respectively. Although the results shown in the tables are for these two situations, the same comparison has been carried out for the other two verification cases. For all situations analysed the same trend has been observed, thus the results presented can be considered as illustrative of the verification process performed.

Major discrepancies have been observed for the first instants, where the formation of the boundary layer takes place. However, relative errors between level of refinement $m3$ and $m4$ at the initial instants in all cases have been below 1%. As time marches, differences between the different meshes tends to level out. It has

	$t = 900s$						$t = 1800s$					
	$\bar{T}$	$\epsilon \cdot 10^3$	$\bar{T}_w$	$\epsilon \cdot 10^3$	$\overline{Nu}$	ϵ	$\bar{T}$	$\epsilon \cdot 10^3$	$\bar{T}_w$	$\epsilon \cdot 10^3$	$\overline{Nu}$	ϵ
	$[^\circ C]$	[%]	$[^\circ C]$	[%]	$[-]$	[%]	$[^\circ C]$	[%]	$[^\circ C]$	[%]	$[-]$	[%]
m_1	59.815	3.3	59.107	0.013	281.864	1.91	59.609	3.32	58.869	1.70	268.349	1.10
m_2	59.813	0.83	59.117	0.003	293.618	2.20	59.607	6.71	58.871	1.71	269.231	1.43
m_3	59.813	0.51	59.124	0.015	286.942	0.15	59.607	0.34	58.870	0.68	267.884	0.92
m_4	59.813	-	59.115	-	287.373	-	59.607	-	58.870	-	265.428	-

	$t = 2700s$						$t = 3600s$					
	$\bar{T}$	$\epsilon \cdot 10^3$	$\bar{T}_w$	$\epsilon \cdot 10^3$	$\overline{Nu}$	ϵ	$\bar{T}$	$\epsilon \cdot 10^3$	$\bar{T}_w$	$\epsilon \cdot 10^3$	$\overline{Nu}$	ϵ
	$[^\circ C]$	[%]	$[^\circ C]$	[%]	$[-]$	[%]	$[^\circ C]$	[%]	$[^\circ C]$	[%]	$[-]$	[%]
m_1	59.405	5.42	58.634	14.0	255.947	0.17	59.202	5.81	58.401	6.8	240.376	1.91
m_2	59.403	2.03	58.629	5.80	255.022	0.53	59.199	0.68	58.400	5.4	242.881	0.85
m_3	59.402	0.34	58.629	5.20	256.179	0.07	59.199	0.31	58.398	1.8	243.298	0.68
m_4	59.402	-	58.626	-	256.372	-	59.199	-	58.397		244.956	-

	$t = 4500s$						$t = 5400s$					
	$\bar{T}$	$\epsilon \cdot 10^3$	$\bar{T}_w$	$\epsilon \cdot 10^3$	$\overline{Nu}$	ϵ	$\bar{T}$	$\epsilon \cdot 10^3$	$\bar{T}_w$	$\epsilon \cdot 10^3$	$\overline{Nu}$	ϵ
	$[^\circ C]$	[%]	$[^\circ C]$	[%]	$[-]$	[%]	$[^\circ C]$	[%]	$[^\circ C]$	[%]	$[-]$	[%]
m_1	59.000	7.53	58.108	123	242.596	0.99	58.799	7.50	57.969	29.3	234.081	1.00
m_2	58.997	2.41	58.171	15.1	236.311	1.61	58.795	1.22	57.958	10.3	235.572	1.65
m_3	58.996	0.68	58.179	1.7	239.516	0.30	58.795	0.51	57.949	5.22	230.858	0.38
m_4	58.996	-	58.180	-	240.185	-	58.795	-	57.952	-	231.752	-

	$t = 6300s$						$t = 7200s$					
	$\bar{T}$	$\epsilon \cdot 10^3$	$\bar{T}_w$	$\epsilon \cdot 10^3$	$\overline{Nu}$	ϵ	$\bar{T}$	$\epsilon \cdot 10^3$	$\bar{T}_w$	$\epsilon \cdot 10^3$	$\overline{Nu}$	ϵ
	$[^\circ C]$	[%]	$[^\circ C]$	[%]	$[-]$	[%]	$[^\circ C]$	[%]	$[^\circ C]$	[%]	$[-]$	[%]
m_1	58.599	7.53	57.750	38.1	227.483	2.91	58.400	8.53	57.537	38.0	219.482	0.50
m_2	58.595	1.36	57.736	13.8	222.617	0.71	58.396	2.39	57.523	13.9	220.169	0.81
m_3	58.595	0.68	57.730	3.46	221.756	0.32	58.396	1.71	57.513	3.48	217.964	0.16
m_4	58.595	-	58.728		221.049	-	58.395	-	57.515		218.393	-

Table 5.4: Verification. Average fluid temperature, wall temperature at the liquid-solid interface and Nusselt number. Comparison results between different levels of refinement at different instants for *case v2*.

	$t = 900s$						$t = 1800s$					
	$\bar{T}$	$\epsilon \cdot 10^3$	$\bar{T}_w$	$\epsilon \cdot 10^3$	$\overline{Nu}$	ϵ	$\bar{T}$	$\epsilon \cdot 10^3$	$\bar{T}_w$	$\epsilon \cdot 10^3$	$\overline{Nu}$	ϵ
	$[^\circ C]$	[%]	$[^\circ C]$	[%]	$[-]$	[%]	$[^\circ C]$	[%]	$[^\circ C]$	[%]	$[-]$	[%]
m_1	59.903	2.84	59.520	10.08	366.679	3.81	59.792	1.672	59.411	20.19	368.281	1.93
m_2	59.903	2.17	59.519	11.76	378.163	0.79	59.791	0.84	59.419	6.731	373.907	0.43
m_3	59.902	0.50	59.531	8.40	379.700	0.39	59.792	0.67	59.420	5.04	374.117	0.37
m_4	59.902	-	59.526	-	381.184	-	59.791	-	59.423	-	375.520	-
	$t = 2700s$						$t = 3600s$					
	$\bar{T}$	$\epsilon \cdot 10^3$	$\bar{T}_w$	$\epsilon \cdot 10^3$	$\overline{Nu}$	ϵ	$\bar{T}$	$\epsilon \cdot 10^3$	$\bar{T}_w$	$\epsilon \cdot 10^3$	$\overline{Nu}$	ϵ
	$[^\circ C]$	[%]	$[^\circ C]$	[%]	$[-]$	[%]	$[^\circ C]$	[%]	$[^\circ C]$	[%]	$[-]$	[%]
m_1	59.681	1.340	59.297	25.29	364.851	2.03	59.571	1.175	59.183	1.520	357.577	2.25
m_2	59.681	0.670	59.293	32.03	366.837	1.49	59.571	0.839	59.180	2.027	361.461	1.18
m_3	59.681	0.503	59.307	8.430	371.944	0.13	59.571	0.504	59.191	1.689	363.071	0.74
m_4	59.681	–	59.312	–	372.422	–	59.571	–	59.192	–	365.789	–
	$t = 4500s$						$t = 5400s$					
	$\bar{T}$	$\epsilon \cdot 10^3$	$\bar{T}_w$	$\epsilon \cdot 10^3$	$\overline{Nu}$	ϵ	$\bar{T}$	ϵ	$\bar{T}_w$	$\epsilon \cdot 10^3$	$\overline{Nu}$	ϵ
	$[^\circ C]$	[%]	$[^\circ C]$	[%]	$[-]$	[%]	$[^\circ C]$	[%]	$[^\circ C]$	[%]	$[-]$	[%]
m_1	59.462	2.691	59.063	6.772	352.192	1.15	59.352	1.348	58.956	0.680	349.082	1.83
m_2	59.461	1.010	59.065	3.326	354.165	0.59	59.352	1.023	58.949	11.87	348.007	1.49
m_3	59.461	0.673	59.066	1.693	355.907	0.11	59.352	0.505	58.948	13.57	344.981	0.62
m_4	59.461	–	59.067	–	356.286	–	59.352	–	58.956	–	342.903	–
	$t = 6300s$						$t = 7200s$					
	$\bar{T}$	$\epsilon \cdot 10^3$	$\bar{T}_w$	$\epsilon \cdot 10^3$	$\overline{Nu}$	ϵ	$\bar{T}$	$\epsilon \cdot 10^3$	$\bar{T}_w$	$\epsilon \cdot 10^3$	$\overline{Nu}$	ϵ
	$[^\circ C]$	[%]	$[^\circ C]$	[%]	$[-]$	[%]	$[^\circ C]$	[%]	$[^\circ C]$	[%]	$[-]$	[%]
m_1	59.243	2.700	58.843	0.339	344.082	1.60	59.135	2.367	58.740	34.10	342.082	2.94
m_2	59.243	1.519	58.835	13.70	335.034	1.07	59.134	1.352	58.720	17.03	330.850	0.43
m_3	59.243	0.675	58.842	1.189	336.600	0.61	59.134	0.673	58.720	16.30	333.746	0.44
m_4	59.242	–	58.843	–	338.653	–	59.134	–	58.730	-	332.299	–

Table 5.5: Verification. Average fluid temperature, wall temperature at the liquid-solid interface and Nusselt number. Comparison results between different levels of refinement at different instants for *case v4*.

been found that the third level of discretisation (grids denoted as m_3 in Table 5.3) provides a good compromise between the computational time to simulate the whole cooling process of the tank and the accuracy of the results. Taking into account the analysis performed, the results presented in this work have been obtained with the third level of refinement (m_3).

5.4.4 A note on the fluid structure

The transient natural convection phenomena taking place inside the storage tank is illustrated in Figs. 5.4 to 5.7. In these figures, the transient evolution of temperatures and streamtraces at different instants of the cooling process, corresponding with one of the cases analysed, are shown. The case selected to illustrate this process is defined by $Ra = 5.986 \cdot 10^{11}$, $H/D = 1$ and $\widehat{U} = 11.6$. In all the figures, variables are given in non-dimensional form.

In Figs. 5.4 and 5.5 it is shown how at the first instants, when the transient convection starts, a boundary layer develops rapidly at the vertical wall. At the same time, the cooled fluid near the wall travels down and moves along the bottom wall forming waves ($\tau = 2.6 \cdot 10^{-5}$). These waves of cooled fluid move towards the centre of the tank forming a crest that interacts with the fluid at the core. When the perturbation arrives to the centre of the tank, it losts its momentum, gradually, and turns back to the vertical wall. At this point, the reverse wave interacts again, with the cooled fluid descending along the vertical wall. This movement of the cold intrusion of fluid at the bottom of the tank, back and forth like a wave motion, interacting with the surrounding fluid and with newly cold fluid at the wall, until it dissipates, complicates the flow pattern during these first instants.

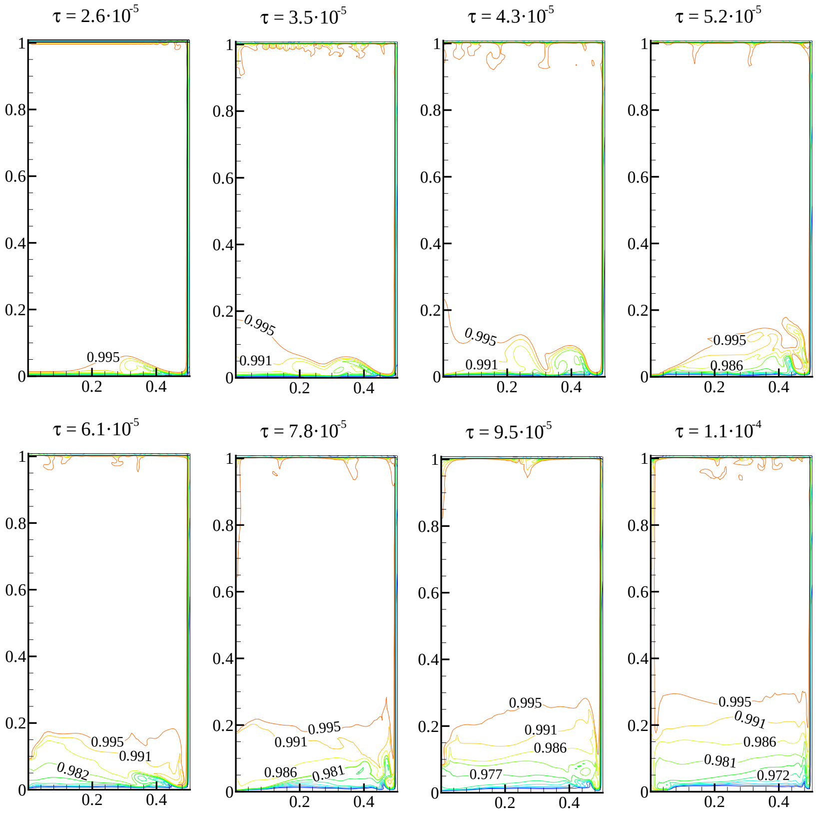

Figure 5.4: Transient evolution of the fluid inside the storage tank. Temperature contour. $\tau = 2.6 \cdot 10^{-5}$ to $\tau = 1.1 \cdot 10^{-4}$. $Ra = 5.986 \cdot 10^{11}$, $H/D = 1$, and $\widehat{U} = 11.6$.

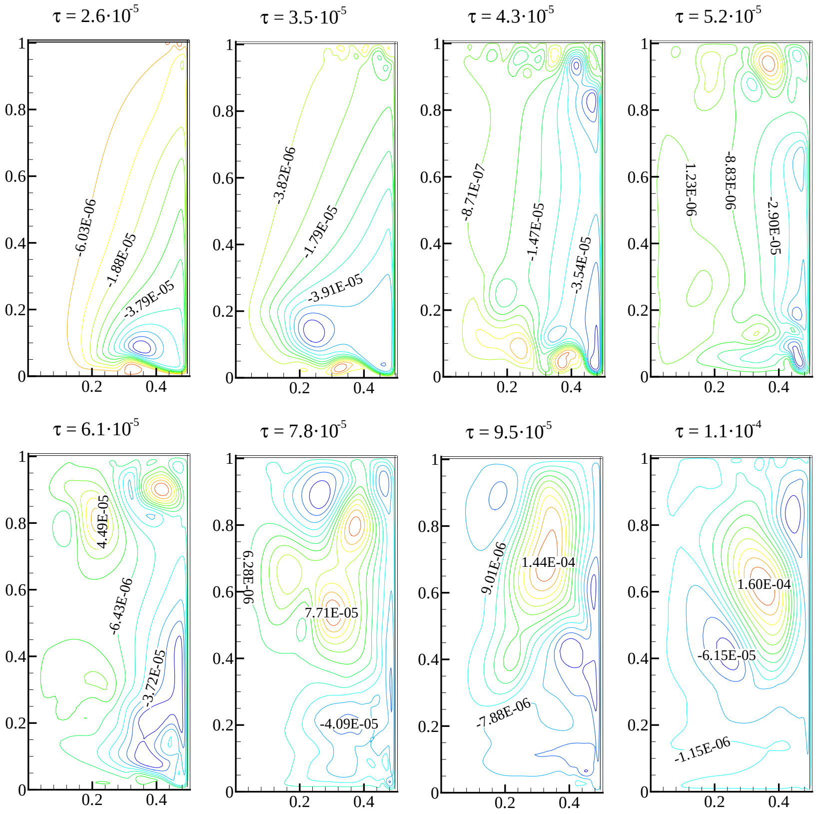

Figure 5.5: Transient evolution of the fluid inside the storage tank. Streamtraces contour. $\tau = 2.6 \cdot 10^{-5}$ to $\tau = 1.1 \cdot 10^{-4}$. $Ra = 5.986 \cdot 10^{11}$, $H/D = 1$, and $\widehat{U} = 11.6$.

The process of wave motion continues just a few instants, but due to the mixing between the cold stream travelling down and the surrounding fluid at the bottom, the layers of cold fluid intruding at the bottom increase their temperature, until their motion vanishes and, begins to generate the stratification of the fluid inside the tank (see $\tau = 6.1 \cdot 10^{-5}$ to $\tau = 1.1 \cdot 10^{-4}$ in Figs. 5.4 and 5.5).

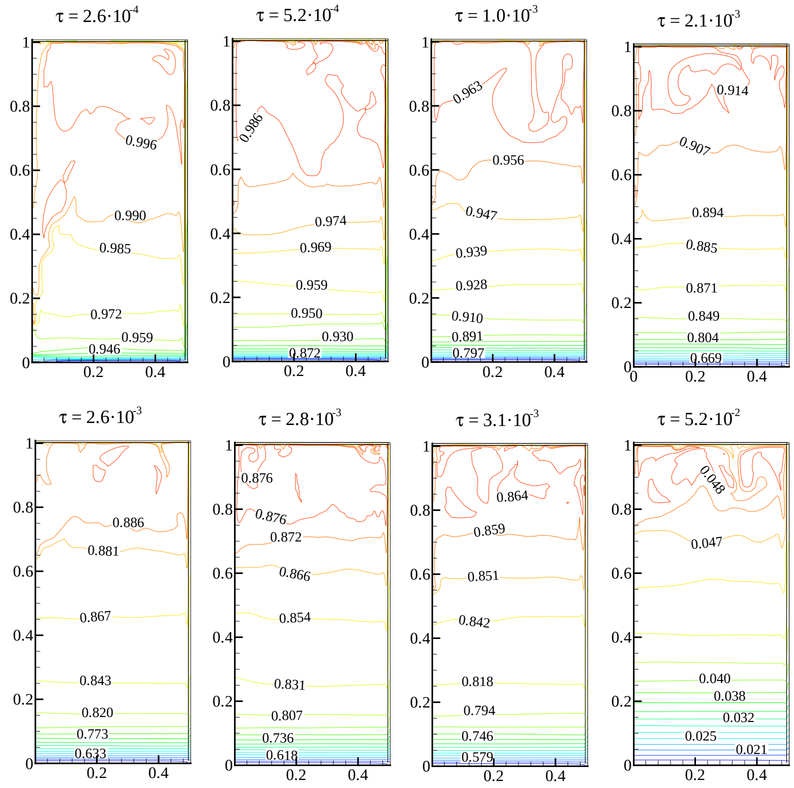

Figure 5.6: Transient evolution of the fluid inside the tank. Temperature contour. $\tau = 2.6 \cdot 10^{-4}$ to $\tau = 5.2 \cdot 10^{-2}$. $Ra = 5.986 \cdot 10^{11}$, $H/D = 1$, and $\widehat{U} = 11.6$.

As the interaction between the cold fluid and that remaining at the core evolves, the stratification of the fluid temperature approach to a quasi-steady regime (Figs. 5.6 and 5.7). In this process, from bottom to top, the tank is filled with layers of fluid at different temperature. As the driving buoyancy decreases ($\tau = 2.6 \cdot 10^{-4}$ to $\tau = 2.8 \cdot 10^{-3}$), the development of the stratification advances at a progressive reduced rate, until this quasi-steady stratification is reached. A similar quasi-steady regime has been reported before by [10] and [13]. The first, studied the transient evolution of a fluid in a vertical cylinder after a suddenly decrease of the temperature in the vertical wall, while the latter studied the transient process of heating a fluid inside a tank under a constant heat flux at the vertical walls. In both studies, top and bottom walls were considered adiabatic.

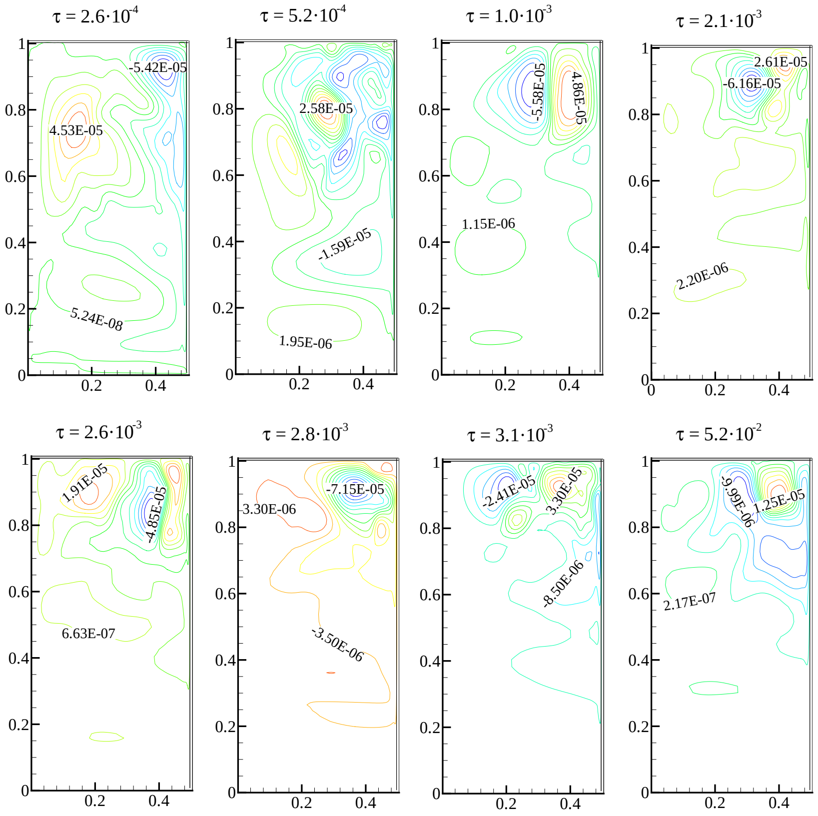

Figure 5.7: Transient evolution of the fluid inside the storage tank. Streamtraces contour. $\tau = 2.6 \cdot 10^{-4}$ to $\tau = 5.2 \cdot 10^{-2}$. $Ra = 5.986 \cdot 10^{11}$, $H/D = 1$, and $\widehat{U} = 11.6$.

For the case shown as an example of the transient evolution of the fluid, this transition occurs around $\tau = 2.8 \cdot 10^{-3}$. At this instant, two regions are clearly formed, a region of stratified fluid at most of the 75% of the bottom part of the tank, while at the top of the tank, there is a wide region of fluid nearly mixed. This mixed region at the top part of the tank, was not reported by [10]. In that case, bottom and top walls were adiabatic, and heat transfer was taking place only at the vertical wall. In the present study, as the top of the tank is not adiabatic, the heat transfer at this region is still intense during the whole cooling process, promoting the mixing of the fluid around that zone. The quasi-steady regime remains until the fluid inside the storage is completed cooled ($\tau = 3.1 \cdot 10^{-3}$ to $\tau = 5.2 \cdot 10^{-2}$). During this stage, which represent about the 94% of the cooling process, the thermal layer becomes thicker due to the decrease of the temperature difference between the wall and the fluid inside the cylinder.

5.4.5 Results of the numerical experiments for one-level global model

In order to evaluate the dimensionless heat transfer coefficient, $\overline{Nu}$, that characterise the heat losses through the lateral, top and bottom walls at each time step, the results of the numerical simulations have been post-processed in the following manner:

$$\begin{aligned}\overline{Nu} = \frac{hH}{k} = \quad & \frac{1}{(\overline{\Theta} - \overline{\Theta}_w)S}\Bigg[- \int\limits_{\partial\Omega_T} \left(\frac{\partial\Theta}{\partial z^*}\right)_T dS \\ & - \int\limits_{\partial\Omega_H} \left(\frac{\partial\Theta}{\partial r^*}\right)_H dS \\ & + \int\limits_{\partial\Omega_B} \left(\frac{\partial\Theta}{\partial z^*}\right)_B dS \Bigg]\end{aligned} \tag{5.31}$$

The mean fluid temperature $\overline{\Theta}$ has been evaluated by Eqn. 5.30 and the mean temperature at the interface of the fluid and solid walls as:

$$\overline{\Theta}_w = \frac{1}{S}\Bigg[\int\limits_{\partial\Omega_T} \Theta_{wT} dS + \int\limits_{\partial\Omega_H} \Theta_{wH} dS + \int\limits_{\partial\Omega_B} \Theta_{wB} dS \Bigg] \tag{5.32}$$

The average heat transfer coefficient

According to the non-dimensional analysis done in section 5.4.1, the Nusselt number can be expressed in terms of the non-dimensional groups τ, Ra, H/D, $\widehat{U}$ and Pr. In the present work, as the fluid considered is only water, the dependence with the Prandtl number, Pr, in the studied range of relevant parameters has been implicitly considered. This treatment can be assumed because in the working range studied, the fluid properties vary slightly with temperature, thus variations can be considered within the Rayleigh number ($Ra = Gr \cdot Pr$). There are some works in the literature that validate this treatment. The influence of the Prandtl number, among other parameters, in the cooling process of a fluid in a cylindrical enclosure after a step change in the vertical and bottom walls temperature was studied by [11]. In the

constant	Value	st. deviation
C_1	4.5851	0.15192
C_2	-0.1686	0.00018
C_3	0.0686	0.00122
C_4	0.5304	0.00257
C_5	0.1981	0.00039

Table 5.6: Results from the curve-fitting. Values of the constants and their standard deviations for the mean Nusselt number non-linear scaling relation (Eqn. 5.33). Values of the constants have been obtained by means of a least-square curve-fitting algorithm.

study, a range of $Pr = 1 \div 1000$ was considered, noting not significant influence of this parameter in the Nusselt number at the bottom wall, while no influence was detected for the Nusselt at the lateral wall. However, the validity of this treatment, i.e. the influence of the Pr number on the $\overline{Nu}$ number, is commented further.

Taking into account the aforementioned hypothesis, the following dependence for the Nusselt number has been proposed:

$$\overline{Nu} = C_1\, \tau^{C_2}\, Ra^{C_3}\, \widehat{U}^{C_4}\, (H/D)^{C_5} \tag{5.33}$$

The data set from the several computations carried out has been fitted to the above scaling relation proposed for the Nusselt number. The fitting process performed in order to find the values of the constants has been done by means of the *GNU Regression, Econometrics and Time-series Library (gretl)* [16]. This library offers a full range of least-squares based estimators, including two-stage least squares and nonlinear least squares data fit, among other possibilities. The actual fitting process has been done using the Levenberg-Marquardt algorithm [17] implemented in this library. This method provides the solution to the non-linear function, minimising the sum of the squares of the deviations. From the curve-fitting, the constants in scaling relation (5.33) have arisen:

$$\overline{Nu} = 4.585\, \tau^{-0.1686}\, Ra^{0.0686}\, (H/D)^{0.53}\, \widehat{U}^{0.1981} \tag{5.34}$$

In Table 5.6 the values of each constant together with its standard deviation are given. Scaling relation (5.34) has been shown a good agreement with all the data set with a goodness of the fit of $R^2 = 0.994$, as can be observed in Fig. 5.8(a). In the figure, raw data and results from the correlation have been arranged in order to express all the data as a function of the non-dimensional time (τ). In Fig. 5.8(b)

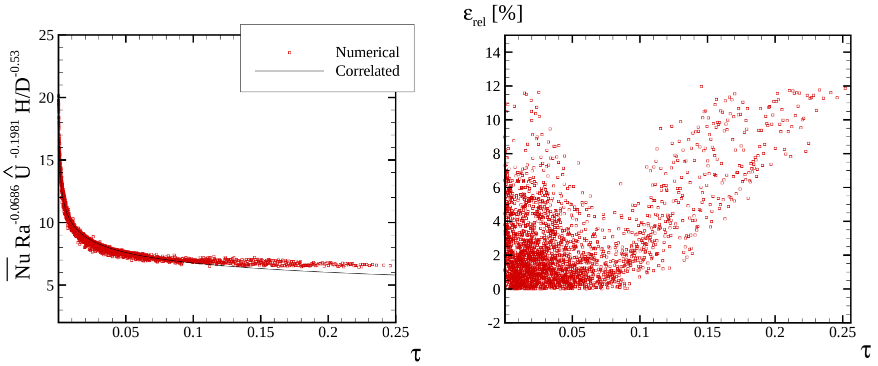

(a)

(b)

Figure 5.8: Results from the curve fitting. Nusselt number. (a) Comparison between fitted data and correlated obtained. (b) Relative errors between raw data and correlated results with Eqn. 5.34.

the relative errors between the fitted data and results from the correlation are also shown. The maximum relative error has been found below 12% and the average relative error is in the order of 2.7%. Major discrepancies have been obtained for large values of the non-dimensional time. These values correspond with the cases with the largest cooling time (lowest aspect ratios H/D and highest non-dimensional overall heat transfer coefficient $\widehat{U}$) which are in limits of the studied range, and the number of samples to be correlated were just a few.

Figure 5.9 shows the raw data from simulations as a function of the non-dimensional time for different Pr numbers in the range of study. The data has been arranged by using the scaling relations for Ra, $\widehat{U}$ and H/D non-dimensional numbers. As can be observed, there is no dependence of the mean $\overline{Nu}$ number on Pr. The six curves corresponding with each of the Pr numbers considered collapse into the same curve. Taking into account these results, the hypothesis of neglecting the influence of the Pr number on the Nusselt number can be assumed, at least within the Pr number range, Pr = $3.83 \div 5.61$.

The transient temperature distribution

The transient evolution of the mean fluid temperature can be obtained from the resolution of the differential equation for the one-temperature level model (global balance, Eqn. 5.14). Alternatively, it is proposed an scaling relation of the kind:

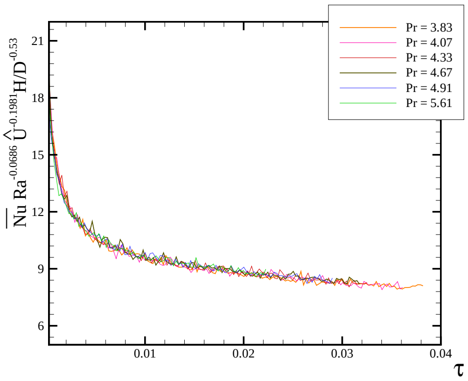

Figure 5.9: Results of the curve fitting. Influence of the Pr number in the average Nusselt number, $\overline{Nu}$.

$$\overline{\Theta} = \exp(C_6 \tau Ra^{C_7} \widehat{U}^{C_8} (H/D)^{C_9}) \tag{5.35}$$

Following the same procedure as for the average Nusselt number, the mean fluid temperature inside the tank obtained from the numerical results has been adjusted. The curve fitting gives:

$$\bar{\Theta} = \exp(-7.506\,\tau\, Ra^{-0.00844}\, H/D^{0.815}\, \widehat{U}^{0.959}) \tag{5.36}$$

The values of the scaling relation constants together with their standard deviation are given in Table 5.7. In Fig. 5.10(a), the raw data and results of the correlation 5.36 as a function of the non-dimensional groups identified are compared, while in Fig. 5.10(b) the relative error between numerical simulations and values from the correlation are given. As can be observed in both figures, all data correlates quite well, with a goodness of the fit of $R^2 = 0.9996$. The maximum relative error obtained has been less than 6.8% and the mean relative error around 1.23%.

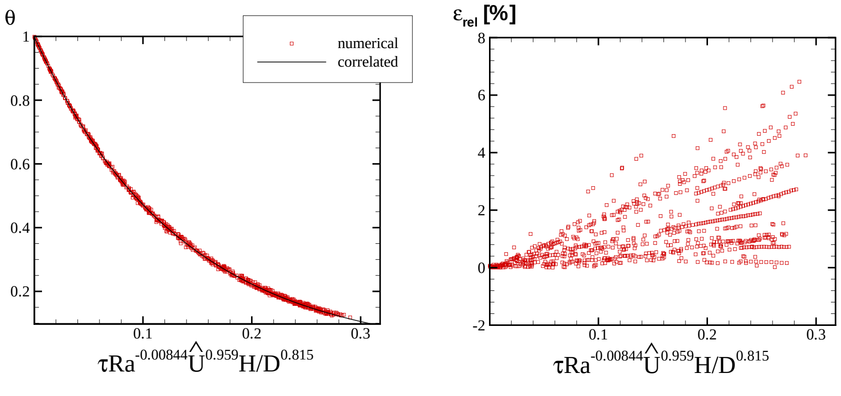

(a) (b)

Figure 5.10: Results of the curve fitting. Comparison between transient fluid mean temperature obtained numerically and correlated. (a) Numerical and correlated non-dimensional fluid temperature plotted against $\left(\tau Ra^{-0.00844}\widehat{U}^{0.959}H/D^{0.815}\right)$. (b) Relative errors between raw data and correlation (5.36).

Table 5.7: Results of the curve-fitting. Values of the constants and their deviations for the non-dimensional mean transient temperature scaling relation (Eqn. 5.35) obtained by means of a least-square curve-fitting algorithm.

constant	Value	st. deviation
C_6	-7.506	0.125180
C_7	-0.0084	0.000614
C_8	0.815	0.001259
C_9	0.9587	0.000162

5.5 Methodology for the resolution of the global model

As has been commented in previous sections, the objective of the analysis of the transient cooling process of the tank is twofold: to characterise the cooling process of the fluid and to predict the behaviour of the mean fluid temperature and the heat losses to the environment. The resolution of both, the temperature and the heat losses, is summarised hereafter by means of the application of the global model presented.

From the one-level temperature model represented by Eqn. 5.14 it is possible to evaluate the transient evolution of the mean fluid temperature at the storage tank, if the superficial heat transfer coefficient (h) is known. In section 5.4.5 has been proposed a correlation for the transient mean Nusselt number (Eqn. 5.34). From this expression, at any instant, the heat transfer coefficient can be evaluated as:

$$h = \frac{\overline{Nu}\,k}{H} = 4.58\tau^{-0.1685}\,Ra^{0.0686}\,(H/D)^{0.53}\,\widehat{U}^{0.1981}\,\frac{k}{H} \tag{5.37}$$

The above expression relates the transient evolution of the heat transfer coefficient with the relevant parameters that defines the case. From this expression, the time dependence of the heat transfer coefficient can then be written in a general form as:

$$h = \Pi t^{n} \tag{5.38}$$

where,

$$\Pi = 4.58\,Ra^{0.0686}\,(H/D)^{0.53}\,\widehat{U}^{0.1981}\,\frac{k\,\alpha^{-0.1685}}{H^{0.663}} \tag{5.39}$$

$$n = -0.1685 \tag{5.40}$$

Substituting Eqn. 5.38 in the one-level temperature balance (Eqn. 5.14) the transient mean fluid temperature in the storage tank can be calculated as:

$$\frac{d\overline{T}}{dt} = -\frac{1}{\rho\,c_p\Omega}\,\frac{\overline{U}\Pi\,t^{n}}{\overline{U}+\Pi\,t^{n}}(\overline{T}-T_{env})S \tag{5.41}$$

The differential equation (5.41) can be integrated for the initial conditions ($t=0$, $\overline{T}=T_0$) giving:

$$\overline{T} = T_{env} + (T_0 - T_{env})\exp\left(-\int_{t=0}^{t}\frac{S}{\rho\,c_p\Omega}\,\frac{\overline{U}\Pi\,t^{n}}{\overline{U}+\Pi\,t^{n}}dt\right) \tag{5.42}$$

The analytical solution of the integral term in Eqn. 5.42 gives as result the first hypergeometric function which its regular solution involves an infinite series expansion in factorial notation [18]. Thus, in order to obtain the transient evolution of the temperature inside the storage tank, a numerical integration of the above equation could be computationally less expensive. This can be done by approximating the integral term as a summation, giving:

$$\overline{T} = T_{env} + (T_0 - T_{env}) \exp\left(-\sum_{k=1}^{N} \frac{S}{\rho\, c_p \Omega} \frac{\overline{U} \Pi\, t_k^n}{\overline{U} + \Pi\, t_k^n} \Delta t \right) \tag{5.43}$$

where

$$t_k = \frac{\Delta t}{2} + (k-1)\, \Delta t \qquad \text{and, } N = \frac{t}{\Delta t} \tag{5.44}$$

The results obtained by means of the numerical integration of Eqn. 5.43 and scaling relation (Eqn. 5.36) proposed in the previous section have been compared with the data from numerical results (see Fig. 5.11(a) and 5.11(b)). Cases plotted in both figures have been selected as illustrative results. These cases correspond with: $Ra = 2.36 \cdot 10^{12}$, $\widehat{U} = 1.274$ and $(H/D) = 2$ for Fig. 5.11(a) and with $Ra = 9.5 \cdot 10^{12}$, $\widehat{U} = 8.224$ and $(H/D) = 3.45$ for Fig. 5.11(b). The numerical integration of Eqn. 5.43 has been carried out by using a time step of $\Delta t = 100s$. Smaller time steps have been tested, but differences between results were not significant. As can be observed, the mean temperature evaluated from Eqn.5.43 and the correlation (5.36), agree quite well with numerical simulation results. Maximum differences have been obtained at the final instants of the cooling process, where $\overline{Nu}$ correlation obtained gives the highest discrepancies.

Once the temperature evolution is known, the heat losses of the fluid from the initial instant ($t = 0$) to any time of the cooling process can be evaluated as:

$$Q^{loss}_{t=0\to t} = c_p(T_0 - T_{env}) \left[1 - \exp\left(-\int_{t=0}^{t} \frac{S}{\rho\, c_p \Omega} \frac{\overline{U} \Pi\, t^n}{\overline{U} + \Pi\, t^n} dt \right) \right] \rho\Omega \tag{5.45}$$

where as in the case of the temperature variation, the integral term is approximated numerically as:

$$Q^{loss}_{t=0\to t} = c_p(T_0 - T_{env}) \left[1 - \exp\left(-\sum_{k=1}^{N} \frac{S}{\rho\, c_p \Omega} \frac{\overline{U} \Pi\, t_k^n}{\overline{U} + \Pi\, t_k^n} dt \right) \right] \rho\Omega \tag{5.46}$$

where t_k and N are evaluated as in 5.44.

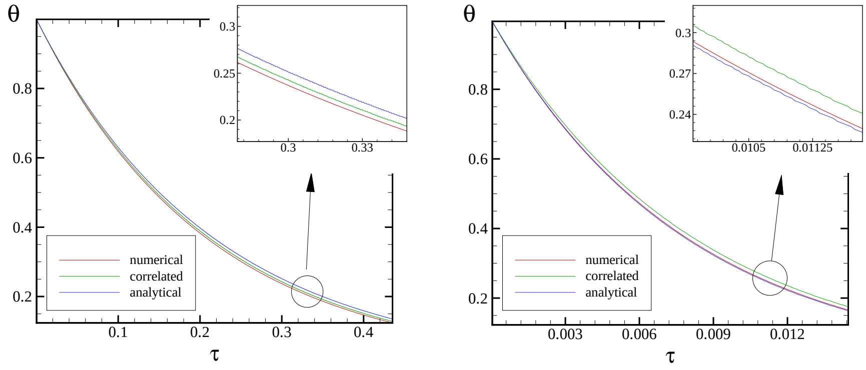

(a) (b)

Figure 5.11: Mean transient temperature of the fluid inside the tank obtained with correlation 5.36 and by numerical integration of analytical expression 5.43. Comparison with numerical results for two illustrative cases: (a) $Ra = 2.36 \cdot 10^{12}$, $\widehat{U} = 1.274$ and $(H/D) = 2$; (b) $Ra = 9.5 \cdot 10^{12}$, $\widehat{U} = 8.224$ and $(H/D) = 3.45$

The methodology for the evaluation of the cooling process of a storage tank under heat losses to the ambient by means of the one-temperature level model is summarised as follows:

1. Define the case and evaluate the relevant parameters Ra, $\widehat{U}$ and H/D.
2. Evaluate the value of the constant Π by means of Eqn. 5.39.
3. Solve numerically Eqn. 5.43 from $t = 0$ to any instant t of the cooling process and obtain the mean temperature. Alternatively, the mean temperature can also be obtained from correlation 5.36.
4. Evaluate heat losses through the tank walls from $t = 0$ to any instant t of the cooling process, by solving numerically Eqn. 5.46.

In order to evaluate heat losses at any instant:

1. Evaluate mean Nusselt number from Eqn. 5.34 at the time of interest.
2. Evaluate the superficial heat transfer coefficient by

$$h = \overline{Nu}\frac{k}{H} \tag{5.47}$$

3. Solve numerically Eqn. 5.43 from $t = 0$ to any instant t of the cooling process and obtain the mean temperature. Alternatively, the mean temperature can also be obtained from correlation 5.36.

4. Evaluate instantaneous heat losses to the ambient as:

$$\dot{Q}_{loss} = \frac{\overline{U}h}{\overline{U}+h}(\overline{T} - T_{env})S \tag{5.48}$$

5.6 Verification of global model. Results and discussion

With the objective of verifying the scaling relations obtained in the working range studied, a new set of cases have been selected. This new set of cases accounted for tank volumes of: $\Omega = 0.16$, 0.3 and 0.5 [m^3], with aspect ratios of: $H/D = 2.05$, 2.77 and 3.2. The insulation of the tank has been set to $\delta_{ins} = 0$ and 2.5 cm. For these cases, initial temperature of $T_0 = 65°C$ and external heat loss coefficient of $h_{ext} = 10$ W/m^2K have been imposed. Ambient temperature and properties of the insulation material have also been varied. Ambient temperatures considered have been of 15 and $20°C$, while polyurethane insulation material has also been considered. All the selected cases were within the range studied for the relevant parameters (Ra, $\widehat{U}$, H/D) except one, which exceeded slightly the maximum Ra number considered in the correlations.

In Figs. 5.12 and 5.13 are shown some of the results obtained with the set of cases. In the figures are represented the cumulative heat losses through the tank walls and the mean fluid temperature estimated compared with the results of the numerical experiments. In addition, in Table 5.8 the mean and maximum relative errors for temperature and heat losses for each of the cases are given. As can be observed, in general, a good prediction of the mean fluid temperature and heat losses has been obtained from the global model. Major discrepancies have been obtained for the cases with the highest non-dimensional overall heat transfer coefficient. These situations corresponded with storage tanks without insulation material, being heat losses the highest.

From this analysis, it can be observed that the application of the proposed methodology together with the correlations for the mean fluid temperature and Nusselt number, are valid within the range of the relevant parameters studied. The predicted results have been shown to be within an acceptable error tolerance considering the limitations of these kind of global models. All the cases studied have been in the range of application for solar domestic hot water storage tanks. Although this is a wide range, the use of these correlations outside the limits considered could fail. In order to extrapolate the current results beyond this range, further studies would be necessary.

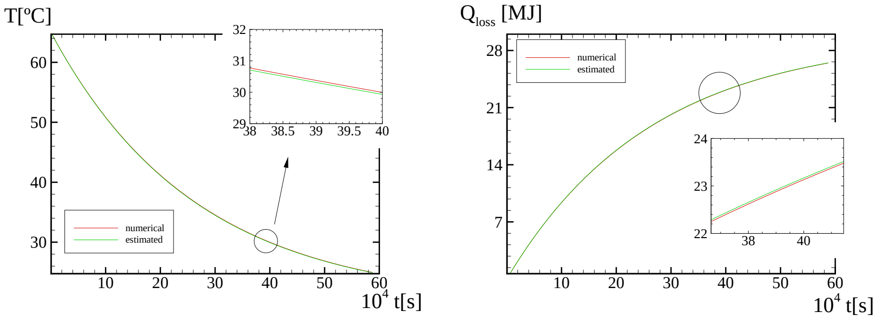

(a)

(b)

Figure 5.12: Verification of the global model. Comparison between numerical experiments and results from the global model. $H/D = 2.77$; $Ra = 2.87 \cdot 10^{12}$; $\widehat{U} = 2.59$. (a) Mean transient temperature of the fluid inside the tank. (b) Cumulative heat losses.

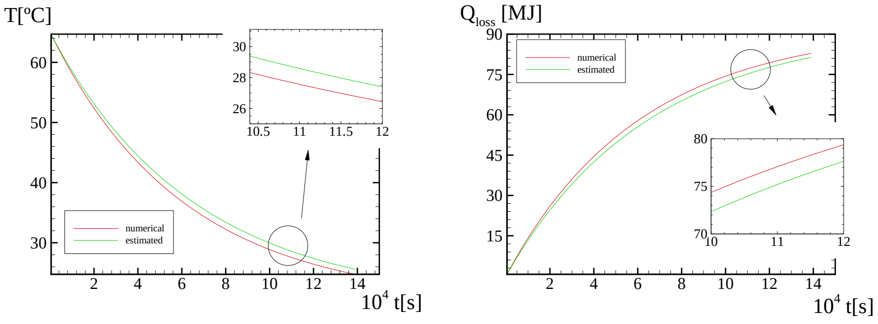

(a)

(b)

Figure 5.13: Verification of the global model. Comparison between numerical experiments and results from the global model. $H/D = 2.05$; $Ra = 4.9 \cdot 10^{12}$; $\widehat{U} = 20.12$. (a) Mean transient temperature of the fluid inside the tank. (b) Cumulative heat losses.

Table 5.8: Verification of the global model. Mean temperature and heat losses through the tank walls maximum and average relative errors between numerical and global model results.

			Maximum relative errors		Average relative errors	
H/D	Ra	$\widehat{U}$	T [%]	Q_{loss} [%]	T [%]	Q_{loss} [%]
2.05	$1.56 \cdot 10^{12}$	2.1	0.16	3.48	0.11	0.62
2.77	$2.87 \cdot 10^{12}$	18.56	1.22	4.39	0.98	1.73
2.77	$2.87 \cdot 10^{12}$	2.59	0.21	6.08	0.17	0.54
3.2	$3.82 \cdot 10^{12}$	20.43	1.21	4.01	0.98	1.55
2.77	$2.87 \cdot 10^{12}$	1.91	0.25	11.98	0.19	0.51
2.05	$2.94 \cdot 10^{12}$	2.56	0.55	3.95	0.16	0.60
2.77	$5.43 \cdot 10^{12}$	3.15	0.24	3.06	0.19	0.56
3.2	$7.18 \cdot 10^{12}$	3.49	0.33	2.58	0.26	0.57
3.2	$7.18 \cdot 10^{12}$	25.16	1.00	4.73	0.81	1.55
3.2	$1.19 \cdot 10^{13}$	4.09	0.29	2.63	0.19	0.52
3.2	$1.19 \cdot 10^{13}$	29.77	0.77	3.98	0.63	1.08
2.05	$4.91 \cdot 10^{12}$	20.11	3.76	10.24	2.86	3.97

5.7 Other possibilities of global models

Sometimes, could be of interest to quantify the heat transfer through each tank wall independently (i.e. top, bottom and lateral). One of the limitation of the procedure outlined in previous sections is that the model does not distinguish between heat losses through top, bottom and lateral walls. In addition, due to the stratification of the temperature inside the tank, the mean fluid temperature can not be used as bulk temperature for the evaluation of the heat transfer coefficients at the top and bottom walls. Then, in an attempt to quantify these losses, the multi-level global model explained in section 5.3 has been used.

From the analysis of the transient evolution of the temperature inside the tank, it has been shown that after the formation of the stratification, the cooling process takes place in a pseudo-steady regime. During this phase, most of the 25 % of the upper part of the tank is filled with water at approximately the same temperature, while a sharpen temperature gradient is observed at almost the 25 % of the bottom part of the tank. Thus, considering the temperature distribution along the vertical height of the tank and that the quasi-steady stratification regime occurs during most of the 90 % of the total cooling time of the tank, three-temperature levels have been considered. For these temperature levels, a distribution of 25, 50 and 25 % of the total volume, respectively, have been assumed.

From the multi-level energy balance (Eqn. 5.1), an energy balance for each temperature level can be written:

$$\begin{aligned}\rho c_p \frac{\partial \bar{T}^{I}}{\partial t}\Omega \quad &+ \quad \dot{m}^{I-II} c_p(\overline{T}^{I} - \overline{T}^{II}) \qquad (5.49)\\ &= \quad -\left(\frac{\overline{U} h_B S_B}{\overline{U} + h_B} + \frac{\overline{U}^{I} h_H^{I} S_H^{I}}{\overline{U}^{I} + h_H^{I}}\right)(\overline{T}^{I} - T_{env})\end{aligned}$$

$$\begin{aligned}\rho c_p \frac{\partial \bar{T}^{II}}{\partial t}\Omega \quad &+ \quad \dot{m}^{I-II} c_p(\overline{T}^{II} - \overline{T}^{I}) + \dot{m}^{II-III} c_p(\overline{T}^{II} - \overline{T}^{III}) \qquad (5.50)\\ &= \quad -\left(\frac{\overline{U}^{II} h_H^{II} S_H^{II}}{\overline{U}^{II} + h_H^{II}}\right)(\overline{T}^{II} - T_{env})\end{aligned}$$

$$\begin{aligned}\rho c_p \frac{\partial \bar{T}^{III}}{\partial t}\Omega \quad &+ \quad \dot{m}^{II-III} c_p(\overline{T}^{III} - \overline{T}^{II}) \qquad (5.51)\\ &= \quad -\left(\frac{\overline{U} h_H S_T}{\overline{U} + h_T} + \frac{\overline{U}^{III} h_H^{III} + S_H^{III}}{\overline{U}^{III} + h_H^{III}}\right)(\overline{T}^{II} - T_{env})\end{aligned}$$

In the above system of equations, temperature levels have been numerated from bottom to top, i.e. the superscript 'I' represents the bottom level of the tank while 'III' represents the top level of the tank. Notice also that in the above formulation it has been assumed that $\overline{U}_T = \overline{U}_B \approx \overline{U}_H = \overline{U}$. In the system, not only the local heat transfer coefficients are unknowns but also the mass flow rates that appears as a consequence of the advective transport between the layers.

5.7.1 Heat transfer scaling relations

According with the definition for the Nusselt number at each wall (Eqns. 5.25 -5.27), and the non-dimensional analysis carried out in section 5.4.1, the Nusselt number at each wall can be written as a function of the relevant parameters identified. From the analysis of the numerical results, different scaling relations have been proposed for evaluating the Nusselt number at each wall. As for the one-temperature level model proposed in previous sections, the numerical data have been adjusted by means of the Levenverg-Marquardt curve-fitting algorithm.

Nusselt number at the bottom wall of the tank

$$Nu_B = 4.3365\tau^{-0.324}Ra^{-0.00549}\widehat{U}^{-0.0928}(H/D)^{-0.1412} \tag{5.52}$$

The average relative error has been in the order of 15% with a goodness of the fit of $R^2 = 0.8734$. Major discrepancies have been obtained at the end of the cooling process, where the absolute value of the Nusselt number is small (in the order of magnitude of 20), being difficult the curve-fitting and relative errors become the highest.

Nusselt number at the top wall of the tank

$$\begin{aligned} Nu_T &= 0.3417Ra^{0.2371}\widehat{U}^{0.1616}(H/D)^{0.3546} \\ \exp &\left(-5.9 \cdot 10^{-4}\tau Ra^{0.2804}\widehat{U}^{0.9243}(H/D)^{0.1307}\right) \end{aligned} \tag{5.53}$$

The mean relative error between the correlation and the numerical results obtained has been about 10.5% with a goodness of the fit of $R^2 = 0.944$. Major discrepancies have been obtained at the first instants of the cooling process, before the development of the stratification. However, discrepancies can also be observed along the whole cooling process between numerical results and correlated ones. These differences can be attributed to the nature of the cooling process near the top wall. At this wall, convective cells are continuously appearing, travelling down until they mixed with the surrounding fluid. This behaviour provokes an oscillatory heat transfer at the top wall and consequently the fluctuation of the Nusselt number. These fluctuations can not be described with the correlation, thus, it can be interpreted as the mean behaviour of the Nusselt number at top wall.

Nusselt number at lateral wall

The transient nature of the Nusselt number at the vertical wall is further complicated. At the beginning of the cooling process, the mean Nusselt number tends to increase with the time until a maximum value is reached. This increasing in the magnitude of the Nusselt number takes places during the formation of the boundary layer and development of the stratification in the tank. After that, the mean Nusselt number decreases continuously with the time. This process is illustrated in Fig. 5.14 for one of the cases solved.

Table 5.9: Three-temperature level model. Results from the curve-fitting adjust for each part of the Nusselt number scaling relation at each temperature level.

Level	zone	Goodness of fit R^2	mean error $\bar{\varepsilon}[\%]$
I	z1	0.9787	3.33
	z2	0.9756	3.77
II	z1	0.9759	3.94
	z2	0.9823	3.84
III	-	0.9805	4.54

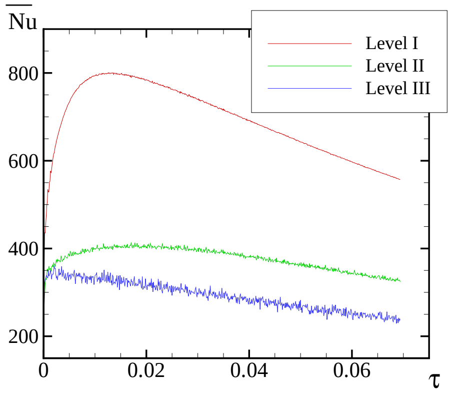

Figure 5.14: Transient evolution of the mean Nusselt number at the vertical wall at each temperature level $Ra = 2.395 \cdot 10^{12}$, $\widehat{U} = 3.045$ and $(H/D) = 2$

Considering the complex behaviour of the Nusselt number, it is easy to devise that to find an appropriate scaling relation that describes its transient evolution could be cumbersome. In order to overcome this difficulty Nusselt numbers behaviour for temperature level I and II have been described by means of a curve divided into two zones (hereafter denoted as subscripts z_1 and z_2). For each zone, results have been fitted giving as results the expressions shown below. Details of the curve-fitting are given in Table 5.9.

Nusselt number at temperature-level I

$$\begin{aligned}\overline{Nu}^{I}_{H,z1} &= 0.795493\tau^{0.139}Ra^{0.2581}\widehat{U}^{0.149}(H/D)^{-0.011}\\ \overline{Nu}^{I}_{H,z2} &= 0.6756Ra^{0.2499}\widehat{U}^{0.051}(H/D)^{-0.0539}\\ &\quad \exp(-7.56\cdot 10^{-3}\tau Ra^{0.2}\widehat{U}^{0.735}(H/D)^{0.25})\\ \overline{Nu}^{I}_{H} &= min\|\overline{Nu}^{I}_{H,z1},\overline{Nu}^{I}_{H,z2}\| \end{aligned} \tag{5.54}$$

Nusselt number at temperature-level II

$$\begin{aligned}\overline{Nu}^{II}_{H,z1} &= 0.466\tau^{0.0567}Ra^{0.2384}\widehat{U}^{0.1914}(H/D)^{0.0412}\\ \overline{Nu}^{II}_{H,z2} &= 0.4168Ra^{0.2416}\widehat{U}^{0.0476}(H/D)^{0.039}\\ &\quad \exp(-3.08\cdot 10^{-4}\tau Ra^{0.3017}\widehat{U}^{0.6104}(H/D)^{0.3132})\\ \overline{Nu}^{II}_{H} &= min\|\overline{Nu}^{II}_{H,z1},\overline{Nu}^{II}_{H,z2}\| \end{aligned} \tag{5.55}$$

Nusselt number at temperature-level III

$$\begin{aligned}\overline{Nu}^{III}_{H} &= 0.1356Ra^{0.269}\widehat{U}^{0.2041}(H/D)^{-0.0127}\\ &\quad \exp(-4.09\cdot 10^{-4}\tau Ra^{0.294}\widehat{U}^{0.906}(H/D)^{0.1827}) \end{aligned} \tag{5.56}$$

In general, there is good agreement between the Nusselt number obtained from numerical simulations and correlated one. Major discrepancies have been observed at the beginning of the cooling process around the instant where the Nusselt number is the highest. However as can be seen in Table 5.9 in all cases mean relative error has been below 4.5%. As illustrative results, the numerical data and results obtained from correlations for Nusselt number of four of the cases considered are plotted in Fig. 5.15.

Mean fluid temperature scaling relations

As for the one-temperature level model, the mean fluid temperature of each fluid level has been adjusted following an exponential dependence of the kind of Eqn. 5.36. In this case raw data from numerical experiments has been pre-processed to evaluate the mean temperature of each volume of fluid, as:

$$\overline{\Theta}^{I}(\tau) = \frac{1}{0.25\Omega}\int\limits_{2\pi}\int\limits_{R}\int\limits_{0}^{0.25H}\Theta\, rdrd\theta dz \tag{5.57}$$

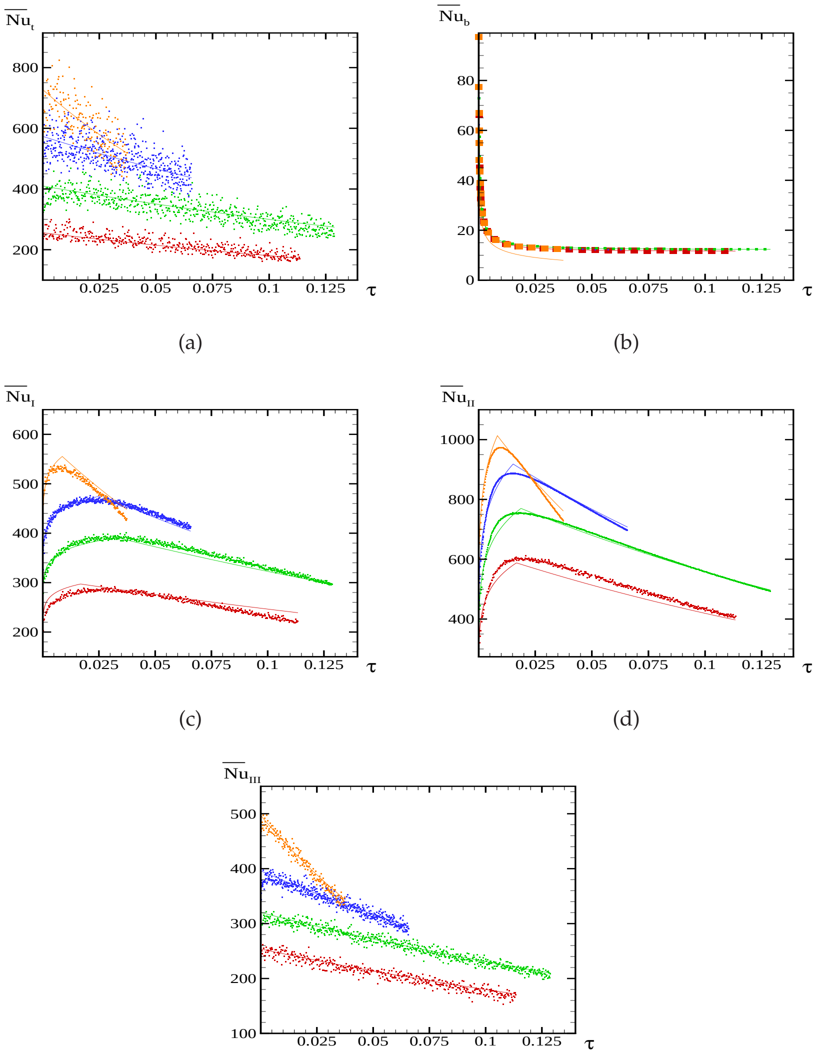

(a) (b)

(c) (d)

(e)

Figure 5.15: Results from the curve-fitting process. Illustrative results of the transient evolution of the mean Nusselt number at the walls according with the three-temperature level global model. Numerical data (dots) and results from correlations (solid line). Red: $H/D = 1$, $Ra = 6 \cdot 10^{11}$, $\widehat{U} = 3.23$; Green: $H/D = 2$, $Ra = 2.4 \cdot 10^{12}$, $\widehat{U} = 1.7$; Blue: $H/D = 3$, $Ra = 5.4 \cdot 10^{12}$, $\widehat{U} = 1.7$; Orange: $H/D = 3.45$, $Ra = 7.1 \cdot 10^{12}$, $\widehat{U} = 3.6$. a) Nu_T; b) Nu_B; c)Nu_H^I; d) Nu_H^{II}; e) Nu_H^{III}

$$\overline{\Theta}^{II}(\tau) = \frac{1}{0.5\Omega} \int\limits_{2\pi} \int\limits_{R} \int\limits_{0.25H}^{0.75H} \Theta \, r dr d\theta dz \tag{5.58}$$

$$\overline{\Theta}^{III}(\tau) = \frac{1}{0.25\Omega} \int\limits_{2\pi} \int\limits_{R} \int\limits_{0.75H}^{H} \Theta \, r dr d\theta dz \tag{5.59}$$

All the data from the several computations have been adjusted with the aid of the curve-fitting library *gretl* [16] to obtain the values of the constants in the scaling relations. The resulting relations read:

Mean fluid temperature at level I

$$\overline{\Theta}^{I} = \exp(-8.008\tau Ra^{-0.00863}\widehat{U}^{0.9997}(H/D)^{0.8064}) \tag{5.60}$$

Mean fluid temperature at level II

$$\overline{\Theta}^{II} = \exp(-7.7299\tau Ra^{-0.01}\widehat{U}^{0.9488}(H/D)^{0.8203}) \tag{5.61}$$

Mean fluid temperature at level III

$$\overline{\Theta}^{III} = \exp(-6.8239\tau Ra^{-0.00591}\widehat{U}^{0.9387}(H/D)^{0.8137}) \tag{5.62}$$

The mean fluid temperature at each level is presented in Fig. 5.16 in terms of $\tau Ra^m \widehat{U}^n H/D^p$, where m, n and p, are the exponents resulting from each correlation (Eqns. 5.60 - 5.62). For the three temperature levels, numerical data correlate quite well. The relative errors obtained has been below 3.5% in all situations, being the greatest differences for temperature level I.

5.7.2 Verification

In order to asseses the validity of the correlations given, as a final step, four of the cases used in section 5.6 for the validation of the one-temperature level global model have been used. The cases selected have been: i) $H/D = 2.77$, $\widehat{U} = 2.59$, $Ra = 2.87 \cdot 10^{12}$; ii) $H/D = 2.77$, $\widehat{U} = 18.56$, $Ra = 2.87 \cdot 10^{12}$; iii) $H/D = 2.77$, $\widehat{U} = 3.15$, $Ra = 5.44 \cdot 10^{12}$ and; iv) $H/D = 3.2$, $\widehat{U} = 4.1$, $Ra = 1.2 \cdot 10^{13}$. For all situations, heat losses through each wall and mean fluid temperature at each level have been predicted by means of the scaling relations and compared with the numerical results.

With the aim of evaluate heat losses at each wall, the following procedure has been applied:

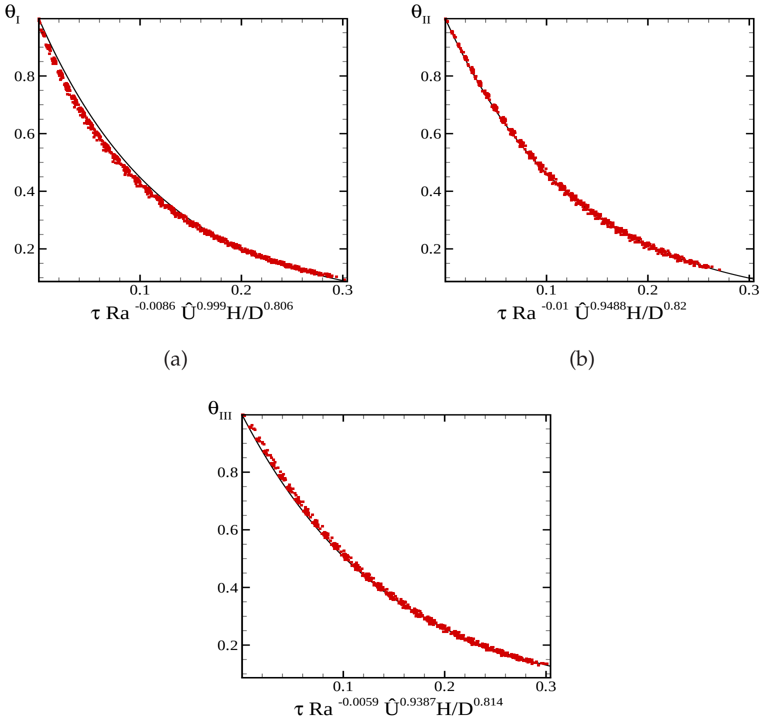

(a)

(b)

(c)

Figure 5.16: Results from the curve-fitting process. Transient evolution of the mean fluid temperature at each level according with the three-temperature level global model. Numerical data (dots) and results from correlations (solid line). a) Temperature level I (Eqn. 5.60); b) Temperature level II (Eqn. 5.61); c) Temperature level III (Eqn. 5.62).

1. First Nusselt numbers have been evaluated using Eqns. 5.52 to 5.56.
2. The heat transfer coefficients between the fluid and the walls have been then calculated as:

$$h^m = \frac{Nu^m\, k}{H} \qquad \text{where } m = (T, B, I, II, III) \tag{5.63}$$

3. At any instant heat losses through the walls have been estimated as:

$$\dot{Q}^m_{loss} = \frac{Uh^m}{U + h^m}(\overline{T^n} - T_{env})S^m \qquad \text{where } m = (T, B, I, II, III) \tag{5.64}$$

   In the above expression the superscript n represents the corresponding temperature level (i.e. $n = I$ for the evaluation of heat losses at the bottom and lateral wall at level I, etc.).

4. Finally, the cumulative heat losses from each wall have been estimated as:

$$Q^m_{loss\;0\to t} = \int_0^t \dot{Q}^m_{loss}(t)dt \qquad \text{where } m = (T, B, I, II, III) \tag{5.65}$$

The numerical and predicted results of the cases considered are given in Table 5.10. In all situations, cumulative heat losses have been evaluated from the initial instant of the cooling process until the 90% of the stored energy has been dissipated to the ambient. Relative differences respect the numerical results are expressed in brackets. In the Table, cumulative heat losses through the vertical wall have been calculated as:

$$Q_{loss\;0\to t} = Q^I_{loss\;0\to t} + Q^{II}_{loss\;0\to t} + Q^{III}_{loss\;0\to t} \tag{5.66}$$

In all cases predicted results agree quite well with the numerical experiments. Relative errors obtained have been below 12%. Major discrepancies have been obtained for the heat losses through the bottom wall. This is in correspondence with the curve-fitting results, where the relative errors for the correlation for the Nusselt number in this wall are the highest. In general, errors obtained with this model are slightly higher than the obtained with the one-level temperature model. The use of more approaches make uncertainties introduced larger than the ones obtained with the one-temperature level model. Although relative error are higher than the simplest model, the prediction of heat losses through each tank wall makes this model useful.

Table 5.10: Verification of the three-temperature level model. Cumulative heat losses predicted. Comparison with numerical results.

			Cumulative heat losses [MJ]					
			Top wall		Bottom wall		Vertical wall	
H/D	$\widehat{U}$	Ra	numerical	predicted	numerical	predicted	numerical	predicted
2.05	2.1	$1.56 \cdot 10^{12}$	2.76	2.66 (4.9)	1.81	2.03 (9.6)	21.97	21.15 (4.83)
2.77	18.56	$2.87 \cdot 10^{12}$	2.35	2.29 (5.9)	0.96	0.94 (6.9)	23.33	23.71 (1.8)
2.77	3.15	$5.44 \cdot 10^{12}$	4.07	3.97 (4.2)	2.55	2.84 (8.5)	43.0	42.5 (1.2)
3.2	4.1	$1.2 \cdot 10^{13}$	5.07	5.01 (4.5)	3.18	3.57 (11.1)	61.9	62.4 (1.1)

5.8 Conclusions

The transient process of cooling-down a fluid initially at rest, by heat transfer through the walls and insulation material has been investigated by means of numerical experiments.

In order to describe the long term behaviour of the fluid inside the storage tank, a global prediction model has been proposed. In the model, the transient behaviour of the fluid has been represented by the mean fluid temperature and the global heat losses through the walls. In order to characterise these heat losses, a non-dimensional analysis has been carried out. This analysis has led to the identification of the significant parameters that define the transient natural convection phenomena inside the tank: the Rayleigh number Ra, the aspect ratio H/D and the non-dimensional overall heat loss coefficient imposed by the boundary conditions of the problem under study. Negligible influence of the Prandtl number, Pr, has been observed within the range considered.

A parametric study has been performed with the aim of finding the correlations that describe the transient behaviour of the Nusselt number. Variations on the different relevant parameters have been taken into account. The situations considered in the study have been within the working range for solar domestic hot water applications. The parametric study consisted in 42 different transient situations. The average Nusselt number and the mean fluid temperature at each instant of all numerical simulations, have been fitted to the scaling relations in terms of the identified relevant parameters arisen from the non-dimensional analysis.

The transient numerical CFD simulations have been shown that as the cooling process evolves there is a development of the thermal stratification from the bottom to the top of the tank. Once the stratification of the fluid is completeley developed, the cooling process takes place in a quasi-steady regime being well distinguished two fluid regions: a clearly stratified zone (with a sharpen temperature gradient) at the bottom and a nearly uniform temperature region at most of 25% of the top volume of the tank.

It has been also shown that the global model methodology proposed to quantify heat losses to the ambient and predict the transient behaviour of the temperature of the fluid are in good agreement with the numerical results. The overall heat transfer rate in all situations is well represented by the scaling relations, being relative errors obtained below 12%.

In addition to the model presented, and with the aim of quantifying the heat losses through each tank wall independently, an extension of the global model has been proposed. In this case three-temperature levels have been considered. Correlations for the Nusselt number at each wall have been obtained from the numerical data. Numerical correlations proposed have been shown a good agreement with the raw data. However, predictions obtained with this model show relative errors slightly greater than those obtained with the one-temperature level model.

The transient problem studied, i.e. heat losses through the top, bottom and lateral walls considering the tank envelope and the insulation material has been out of scope of the up-to-now transient heat transfer studies presented by other authors. In general, previous studies have been limited to heat transfer in the fluid without considering the tanks walls and the insulation material.

Nomenclature

c_p	specific heat at constant pressure ($J/kg\ K$)
D	tank internal diameter (m)
H	tank internal height (m)
h	superficial heat transfer coefficient ($W/m^2\ K$)
k	thermal conductivity ($W/m\ K$)
L_{ref}	reference length (m)
n_r	number of control volumes in radial direction
n_z	number of control volumes in axial direction
Pr	Prandtl number
p	pressure (Pa)
p^*	non-dimensional pressure
r^*	non-dimensional radial distance
S	area (m^2)
T	fluid temperature (K)
$\overline{T}$	mean fluid temperature (K)
$\overline{T}_w$	mean wall temperature (K)
T_{env}	ambient temperature (K)
T_0	initial temperature (K)
ΔT_{ref}	reference temperature difference (K)
t	time (s)
U	overall heat transfer coefficient ($W/m^2\ K$)
$\widehat{U}$	non-dimensional overall heat transfer coefficient

$\dot{Q}_{loss}$	instantaneous heat losses (W)	$\overrightarrow{v}$	velocity vector (m/s)
$\overrightarrow{q}$	heat flux vector (W/m^2)	$\overrightarrow{v^*}$	non-dimensional velocity vector
Ra	Rayleigh number	v_{ref}	reference velocity (m/s)
$\overrightarrow{r}$	position vector (m)	z^*	non-dimensional z-coordinate
$\overrightarrow{r^*}$	non-dimensional position vector		

Greek letters:

α	thermal diffusivity (m^2/s)	ρ	density (kg/m^3)
δ_{ins}	insulation thickness (m)	τ	non-dimensional time
δ_t	wall thickness (m)	θ	azimuthal coordinate
Θ	non-dimensional temperature	Ω	volume (m^3)

Subscripts:

B	tank bottom wall	T	tank top wall
H	tank vertical wall	w	wall

References

[1] G. De Vahl Davis. Natural convection of air in a square cavity: a benchmark numerical solution. *International Journal for Numerical Methods in Fluids*, 3:249–264, 1983.

[2] G.D. Mallison and G. De Vahl Davis. Three-dimensional natural convection in a box: a numerical study. *Journal of Fluid Mechanics*, 83:1–31, 1977.

[3] J. Vierendeels, B. Merci, and E. Dick. Numerical study of convective heat transfer with large temperature differences. *International Journal of Numerical Methods in Heat and Fluid Flow*, 11(4), 2001.

[4] Patterson J. and J. Imberger. Unsteady natural convection in a rectangular cavity. *Journal of Fluids Mechanics*, 100:65–86, 1980.

[5] V.F. Nicolette, K.T. Yang, and J.R. Lloyd. Transient cooling by natural convection in a two dimensional square enclosure. *International Journal of Heat and Mass Transfer*, 28(9):1721–1732, 1985.

[6] J.M. Hyun. Transfer process of thermally stratifying an initially homogeneous fluid in an enclosure. *International Journal of Heat and Mass Transfer*, 27(10):1936–1938, 1984.

[7] W.M. Rosehnow, J.P. Hartnett, and E.N. Ganić, editors. *Handbook of Heat Transfer Fundamentals*, chapter Natural Convection, pages 6–67 –6–68. McGraw-Hill Book Company, 1985.

[8] M.A. Cotter and M.E. Charles. Transient cooling of petroleum by natural convection in cylindrical storage tanks-I. Development and testing the numerical simulator. *International Journal of Heat and Mass Transfer*, 36(8):2165–2174, 1993.

[9] M.A. Cotter and M.E. Charles. Transient cooling of petroleum by natural convection in cylindrical storage tanks-II. Effect of heat transfer coefficient, aspect ratio and temperature-dependent viscocity. *International Journal of Heat and Mass Transfer*, 36(8):2175–2182, 1993.

[10] W. Lin and S.W. Armfield. Direct simulation of natural convection cooling in a vertical circular cylinder. *International Journal of Heat and Mass Transfer*, 42:4117–4130, 1999.

[11] W. Lin and S.W. Armfield. Long-term behaviour of cooling fluid in a vertical cylinder. *International Journal of Heat and Mass Transfer*, 48:53–66, 2005.

[12] De Césaro Oliveski R., A. Krezinger, and H.A. Vielmo. Cooling of cylindrical vertical tanks submitted to natural internal convection. *International Journal of Heat and Mass Transfer*, 46:2015–2026, 2003.

[13] E. Papanicolaou and V. Belessiotis. Transient natural convection in a cylindrical enclosure at high Rayleigh numbers. *International Journal of Heat and Mass Transfer*, 45:1425–1444, 2002.

[14] P.H. Gaskell and A.K.C. Lau. Curvature-compensed convective transport: SMART, a new boundedness-preserving transport algorithm. *International Journal for Numerical Methods in Fluids*, 8:617–641, 1988.

[15] C.D. Pérez-Segarra, A. Oliva, M. Costa, and F. Escanes. Numerical experiments in turbulent natural and mixed convection in internal flows. *International Journal for Numerical Methods for Heat and Fluid Flow*, 5(1):13–33, 1995.

[16] A. Cottrell and R. Lucchetti. Gretl, GNU Regression, Econometrics and Time-series Library, version 1.5.0, 2005.

[17] Marquardt D. An algorithm for least-squares estimation of nonlinear parameters. *SIAM. Journal of Applied Mathematics*, 11:431–441, 1963.

[18] M. Abramowitz and I.A. Stegun, editors. *Handbook of Mathematica Functions with formulas, graphs and, mathematical tables*, chapter 15, "Hypergeometric functions", pages 555–566. New York: Dover, 9 th edition, 1972.

Chapter 6

Concluding remarks and future actions

Thermal storage tanks of liquid water are being used in many engineering applications where energy production and consumption do not match in time, such as solar energy systems. In these applications, a properly design of these devices is a key aspect for the optimum performance of the whole system. In this sense and considering the complex phenomena associated, virtual prototyping of storage tanks is becoming a powerful tool in their design and optimisation.

The main contribution of the present thesis is the resolution of transient problems in cylindrical coordinates geometries applied to the study of transient heat transfer and fluid flow phenomena in storage tanks for solar domestic systems. The detailed simulation of such complex heat transfer phenomena requires a proper discretisation of the governing equations on both space and time. Hence, attention have also been focused in the basic mathematical formulation and numerical tools for the resolution of both heat transfer and fluid flow in three-dimensional cylindrical coordinates.

The main particularities of the discretisation of the governing equations used in these domains have been exposed. Special attention has been dedicated to the treatment of the singularity that appears at the cylinder centre and to the spatial periodicity at the azimuthal direction. In this sense, for the formulation of the singularity at the cylinder centre, where some terms become undefined, different treatments proposed in the literature have been tested. From this analysis, a new approach has been prescribed by evaluating the velocity vector at the axis from the averaging of the cartesian velocity components at the nearest nodes to the centre. On the other hand, as the solver used on the resolution of the system of equations has been intended to be employed on either cartesian or cylindrical domains, an explicit the boundary condition formulation at the azimuthal direction has been imposed. The formulation of this special boundary condition has been explained in detail *Chapter 2*.

In the process of development or improvement of a CFD code, it is important to submit the code and the numerical solutions to a rigorous process of verification. In this sense, the post-processing procedure followed in the assessment of the numerical solutions, in order to quantify errors and uncertainties, has been also exposed. This post-processing procedure implemented at CTTC, is based on the generalised Richardson extrapolations for *h-refinement* studies and on the Grid Convergence Index (*GCI*).

In *Chapter 3*, the techniques outlined in the previous chapter have been applied to the resolution of different axisymmetric and 3D test cases in cylindrical coordinates. Two main aspects have been discussed: i) the usefulness of the aforementioned post-processing procedure in the process of code development pointing out its utility in the selection of the appropriate discretisation grid, numerical schemes or in detecting possible programming bugs and, ii) its usefulness in the verification of the numerical solutions, defining their uncertainty due to discretisation and order of accuracy.

In two of the test cases presented, both with analytical solution known, the estimates obtained from the verification procedure have been useful to give criteria about its appropriateness in the verification of the numerical solutions in three-dimensional cylindrical coordinates. The verified solutions of all these tests cases have been presented. In all situations, the estimates obtained from the verification process have shown a good behaviour, i.e. an order of accuracy around its theoretical value with a high percentage of Richardson nodes. These verified numerical solutions, together with their uncertainty estimates, would be an useful tool to be employed as reference solutions during the process of verification of CFD codes.

Main contributions of this thesis to the study of the transient heat transfer and fluid dynamics phenomena in storage tanks have been reported in *Chapters 4 and 5*. Partial conclusions on these topics have been given in each chapter. However, the most important ones are highlighted hereafter. *Chapter 4* have been focused on thermal stratification studies in storage tanks on both, horizontal and vertical configurations. The studies have accounted for the influence of the mass flow rate during the unloading process of a tank forming part of a thermosyphon system and the influence of different inlet and initial conditions on the stratification process of a vertical storage with a manifold diffuser, during its loading phase. Both situations have been tested virtually by means of detailed multidimensional computational fluid dynamics (CFD). The methodology followed from the definition of the problem, the assumption of a mathematical model, its conversion into a numerical one, and the analysis of the numerical solutions obtained have been also shown.

Parallel multi-block techniques have been used for the resolution of the withdrawn process of the horizontal storage tanks with asymmetric ports, under different mass flow rates. The detailed study of this configuration have demanded a large amount of computational resources (three-dimensional domains) to obtain accurate enough results. Taking advantage of “low cost” parallel computational infrastructures (Beowulf clusters) at CTTC, the use of these kind of techniques have been useful to deal with the virtual prototyping of the tanks with a reasonable cost of CPU time. The computational performance of the algorithm, based on the domain decomposition method, has been shown pointing out the computational savings obtained for this kind of situations.

A review about the state-of-the-art in the quantification of the degree of thermal stratification in storage tanks, has also been done in *Chapter 4*. Some of the methods proposed in the literature have been tested and, based on the analysis of the results, a new exergy-based parameter has been proposed. The non-dimensional exergy parameter proposed have been capable of reflecting quantitatively the thermal performance of the storage tanks and has been shown its usefulness in the assessment of thermal storage designs. Exergy-based analysis have been proven a useful tool for quantifying the quality of the energy stored in the tank, providing a method for the thermal stratification studies where energy-based analyses fails.

In *Chapter 5*, the performance of storage tanks submitted to heat losses to the ambient during its static mode of operation has been numerically studied. Transient convection has been parameterised by means of a non-dimensional analysis and a parametric study has been carried out in terms of the significant parameters identified. Rayleigh number and aspect ratio (H/D) have been confirmed as significant parameters governing natural convection inside enclosures, as well as the non-dimensional wall heat transfer coefficient ($\widehat{U}$) have been identified as a relevant parameter to account for the tank envelope influence. The Prandtl number which has also been identified as another relevant parameter did not influence the Nusselt number within the range of parameters considered.

A global model based on a one-temperature level has been proposed as a prediction model to evaluate the long-term performance of the fluid inside the storage tank. A parametric study has been performed including different situations within the working range of storage tanks for solar domestic hot water systems, with the aim of finding the correlations to feed the prediction model. The analysis of the results have led to the development of non-linear correlations for Nu number and for the mean temperature inside the tank.

These correlations have been verified and tested against the simulated performance of the tanks. It has been also shown that the global model methodology proposed to quantify heat losses to the ambient and predict the transient behaviour of the temperature of the fluid is in good agreement with the numerical results. The overall heat transfer rate in all situations is well represented by the scaling relations. Correlations such as those developed in the present thesis can be useful for the design and prediction of the behaviour of storage tanks. However, they should be applied with due regard for the assumptions on which they rest.

Future actions

The design and optimistion of the thermal performance of storage tanks, including the transient study of heat transfer and fluid flow phenomena taking place in these devices such as the carried out in the present thesis, would require of further research works.

Domestic hot water storage tanks are often designed with internal wrapped-around heat exchangers for the collector loop and also for the load loop. It would be intersting to study the influence of such internal elements in the degree of thermal stratification and by consequence, its influence in the overall performance of the system. In this sense, the use of more advanced computational tools for complex geometries (unstructured meshes) would enable this kind of studies. These techniques would allow also the study of the influece of convex top and bottom walls, non-axisymmetric diffusers, among other internal elements that can not be described by means of cylindrical structured meshes.

Regarding to the mathematical modelling of the mixed convection phenomena in storage tanks, turbulence modelling is expected to be considered in future works. Turbulence might occur at located zones, near the inlet. In this sense, the implementation and assessment of different turbulence models should be carried out in order to choose an appropriate modelisation of this phenomena. Low Reynolds models or zonal *RANS/LES* models would be considered. The selected models should be capable of describe the relaminarisation in the core of the tank. On the other hand, experimental techniques and results of numerical experiments by means of the Direct Numerical Simulation (*DNS*) of the storage should also be considered. *DNS* together with experimental techniques might be used as reliable tools for a clear understanding of turbulence effects in the entrance, to acquire experience about turbulent regime of operation of the tank and thus, to select the most appropriate turbulence models to be used. Although *DNS* would demand, a priori, a large amount of computational resources, its application by using local refinements just in the zones near the inlets is feasible. However, due to the requirements of small time increments, the simulation of the large working periods of the storage or its application to parametric studies could be cumbersome.

New unsteady multi-zonal prediction models for their use in long-term simulations of solar energy systems are expected to be developed. Current prediction global models not only are dependent of a large amount of empirical coefficients, but also are not capable of modelling the mixing effects of the incoming fluid streams. Future research works will be planned in order to account for these effects. In this direction, virtual prototyping of storages with different inlet ports and diffusers, working under different conditions will be carry out. The results of such kind of parametric studies will be used in the modelling of the mixing effects into prediction codes.

Correlations proposed in Chapter 5 for the characterisation of the heat losses to the ambient of storage tanks during the still phase are limited to the range of parameters studied. A generalisation of these results, including dynamic mode of operation might be possible.

With reference to the design of storage tanks, different strategies will be studied in the near future. The influence of different kind of diffusers to enhance stratification is a topic widely treated in the literature. However, considering the variable working conditions of solar energy systems (e.g. variation in solar radiation and, by consequence, variation of the inlet temperature of the fluid), inlet diffuser designs are still far of provide an efficient performance. In this sense, some preliminary results have been obtained with the simulation of a manifold with damping orifices to avoid mixing under adverse working conditions. In spite of this, further numerical and experimental studies will be required for the design and optimisation of those diffusers. Other inlet strategies will be also considered, such as an external multiport inlet with a smart temperature control, to direct inlet fluid to the temperature level most closest to its temperature.

In the same line of promote and enhance stratification of storages tanks is the study of low-flow systems. As has been commented in this thesis, performance is generally improved with the decreasing of the mass flow rate. The magnitude of these improvements together with the study of different kind of inlets will be investigated.

The design of hybrid/latent storage tanks is becoming a promising alternative to improve the storage capacity, the level of stratification and the compactness of these devices. Different works have been also carried out at CTTC as part of an European Reasearch Project. Following this research line, innovative concepts and future designs might be object of future works.